



FACULTY OF SCIENCE AND TECHNOLOGY

MASTER'S THESIS

Study programme/specialisation: Engineering Structures and Materials- Renewable Energy	Spring/ semester, 20 20 ²¹ Open
Author: Jan Koles	
Programme coordinator: Professor Vidar Folke Hansen Supervisor(s):	
Title of master's thesis: 3D printed Aluminium Bronze Microstructure and mechanical properties of a aluminium-bronze alloy	
Credits: 30	
Keywords: Al-bronze Micro-structure Mechanical Properties TEM Direct Energy Deposition	Number of pages: 50 + supplemental material/other: Stavanger, 13.6.2021 date/year

3D printed Aluminium Bronze

Microstructure and mechanical properties of an aluminium-bronze alloy

Jan Koles

June 13, 2021

Abstract

Design and production of the blades is a sophisticated process that needs to be optimized for given permanence of the rotor. Shape of the rotor requires complicated casting. For small series of production it is wise to use 3D printing technology. Aluminium - Bronze as a production material offers good combination of strength, flexibility, corrosion resistance and ease of printing. Micro-structural properties were studied on a specimen printed by robotized direct-energy-deposition machine using 2200W laser. Analysis was carried out on optical microscope, scanning electron microscope and transmission electron microscope. Also X-ray spectroscopy was performed. It was found that the Al bronze contains α Cu and Fe_3Al phase.

Acknowledgments

I would like to thank to Professor Vidar Hansen for all his support and advice. He helped me to conduct this master thesis and extend my current knowledge of the materials.

I also would like to thank senior engineer Mona W. Minde for help with analyzing the samples during the XRD, Wakshun Mekonnen Tucho with preparing samples for TEM and analyzing TEM results, and Johan Andreas Thorkaas for his help in the polishing lab with sample preparation and etching.

It would also not be possible to carry out this work without support of Sture H. Sørli from Nordic Additive Manufacturing AS, who provided me the samples and all the information and pictures from the sample production.

Finally, special thanks belongs to Ole Bjørn Karlsen from Oslo University, who analyzed my sample on SEM, when the UiS SEM was broken.

Contents

1	Theory	9
1.1	Direct Energy Deposition and Powder Bed Fusion	9
1.1.1	Powder Bed Fusion	10
1.1.2	Direct Energy Deposition	10
1.2	Parameters of 3D printing	11
1.2.1	Laser power	11
1.2.2	Print speed	12
1.2.3	Scanning strategy	12
1.2.4	Layer height and Track width	12
1.2.5	Special parameters of 3D print by DED	12
1.2.6	Defects in DED	13
1.3	Aluminium bronze	13
1.3.1	Copper	14
1.3.2	Aluminium	14
1.3.3	Iron	14
1.4	Micro-structure of Aluminium bronze	17
1.4.1	Alpha [α] phase	17
1.4.2	Beta [β] phase	17
1.4.3	alpha + gamma ₂ [$\alpha + \gamma_2$] phase	17
1.4.4	Kappa [κ] phase	18
1.4.5	Iron	18
1.4.6	Dislocations	18
1.5	Hardness testing	20
1.6	Microscope	20
1.6.1	Light microscope	21
1.6.2	Electron microscope	21
1.6.3	Scanning electron microscope	24
1.6.4	Transmission electron microscope	25
1.6.5	X-ray Diffraction (XRD)	26
1.6.6	Indexing of diffraction patterns from TEM and XRD results	26
2	Methodology	28
2.1	Direct Energy Deposition - Sample properties	28
2.2	Sample preparation	31
2.2.1	Cutting	31
2.2.2	Hot Mounting	31
2.2.3	Grinding and polishing	31

2.2.4	Sample preparation for TEM	31
2.2.5	Sample preparation for XRD and the test program	32
2.2.6	Sample preparation for Hardness testing	32
3	Results	35
3.1	Hardness test	35
3.2	XRD results	35
3.3	Results from the light microscope	37
3.3.1	Micro-structure	37
3.4	SEM results	40
3.5	TEM results	40
4	Conclusion	44
4.1	Future work	44
	References	45
A	Appendix	48

List of Figures

1.1	Publications about rapid prototyping, 3d printing, AM and bio-printing according to amount of references per year [2].	9
1.2	Powder bed manufacturing process [3].	10
1.3	DED manufacturing process [4].	11
1.4	Three main scanning strategies: a) Parallel, b) ZigZag, c) Spiral [6].	12
1.5	Description of the printed layers [8].	13
1.6	Phase diagram for CuAl system. For purpose of this work the part around 20at% (9.42wt%) of Al is important [33].	15
1.7	a) heating and cooling curves of iron b) phase transitions [11].	16
1.8	Left phase diagram is for Copper Aluminium Iron (3wt%) and right phase diagram is for Copper Aluminium [14]. Red lines represent Aluminium content of the tested samples.	19
1.9	Section of the Cu-Al phase diagram [32], red line depicts Al content for the tested samples.	19
1.10	Schematic diagrams of A) an edge and B) screw dislocation in an atomic lattice [37]. .	20
1.11	Schematic drawing of Vickers hardness test indenter [29].	20
1.12	Olympus GX53 used during the research. Sample is placed on top deck and the objective lens is located below the sample. Condenser is improving the illumination of the specimen by gathering from the light source and pointing it to the sample [17].	21
1.13	Electron-matter interaction volume and types of signal generated [21].	23
1.14	SEM scheme [22].	24
1.15	TEM (JEM-2100) located at the University of Stavanger and the scheme of TEM [25].	26
1.16	Scheme of Bragg's diffraction condition - sum of length AC and CB is path difference between beams 1' and 2' diffracted from two neighboring atomic planes [27],[28]	27
2.1	Samples from Nordic Additive Manufacturing [21].	29
2.2	SEM image of the Oerlikon powder Metco 51NS [31].	29
2.3	Final product - marine propeller (Photo by: NAM)	30
2.4	Scanning method of the DED samples	30
2.5	Solid samples for XRD measurement - one from sample for each section - XZ, YZ and XY.	32
2.6	Powder preparation for XRD - uppermost picture is grinding and then filtering of the "powder". Middle picture is from saw cutting and the lowest picture is preparation using the file.	33
2.7	Schematic picture of indents on 3 different sections.	34
3.1	XRD results for 3 solid samples and 3 powder samples	36
3.2	Detail XRD results sample 2 - YZ section	36
3.3	A) Photo of the weld pools B) Weld pools on the LM C) Depicted lines of the melt pools for the picture B)	37

3.4	LM picture of the surface with porosity (black particles). Circular pores possibly from shielding gas and non circular from scanning faults.	38
3.5	Larger weld defects 21mm x 4mm.	38
3.6	Different magnification of weld pool boundary - different orientation and larger amount of α Cu phase is probably causing visibility of the boundary.	39
3.7	White parts of the picture are α Cu, dark lamellar are β' and dark dots are pores or κ_1	39
3.8	SEM Surface picture, BSE image and chemical composition from one sample supplied by Oslo university.	40
3.9	Spherical coherent participates in α Cu phase	41
3.10	Typical DP for the α Cu phase. Right DP belongs to the surface (lower picture). In the lower picture, dislocations can be observed. Average a value calculated from multiple DP is 3.66Å.	42
3.11	Surface of the β phase together with diffraction pattern. Average a value was calculated as 1.79Å.	43
A.1	Certificate of the powder used for the production of the tested samples.	48
A.2	Results of the Vickers hardness test - load 5kg for 10s.	49

List of Tables

1.1	Main types of Additive Manufacturing techniques incorporating powder source material.	10
1.2	Classification of Aluminium bronzes according to [32].	14
1.3	Main differences between light microscope, scanning electron microscope and transmission electron microscope [18], [19].	22
2.1	Chemical composition of the powder Metco 51NS.	28
2.2	Grinding and polishing procedure.	31
2.3	Different voltages during electropolishing for TEM.	32
3.1	Measured and calculated angles for different phases.	35

List of Abbreviations

AM	additive manufacturing
BSE	back-scattered electrons
DP	diffraction pattern
DED	direct energy deposition
EBSD	electron backscatter diffraction
EDS	energy-dispersive X-ray spectroscopy
EM	electron microscope
LM	light microscope
NAM	Nordic Additive Manufacturing Raufoss, Norway
PBD	powder bed fusion
SE	secondary electrons
SEM	scanning electron microscope
TEM	transmission electron microscope
XRD	X-ray diffraction

1. Theory

Increasing industry needs in weldability, corrosion resistance, high tensile and yield strengths at different temperature ranges led to development of additive manufacturing (AM). AM is a technology where layers of a material are placed on each other to create final product.

The term “Additive manufacturing” is sometimes connected with rapid prototyping. Such prototypes are often used in industry during testing or for improving an existing product. During production of a prototype the main concern is the production time of the prototype and the price. Final product can be produced by different methods than the original prototype so they can have different mechanical properties. In earlier days the terms Rapid prototyping and additive manufacturing were equivalent. Today these terms are not used together because by some of the AM methods it is possible to produce not only prototypes but also final products with required mechanical properties. Rapid prototyping is therefore one of the sub-categories of AM.

AM is also sometimes called 3D printing. 3D printing is used for creating prototypes for more than 20 years. AM increases possibilities of design, where new ideas can be transformed to real world straight away. With the development of AM methods came also efforts to incorporate this prototyping method into normal production processes. Advantages of AM are the decrease of the weight, decreased material consumption, and lower final prize for sophisticated shapes. There can be savings in machining tools, because the material is added instead of removed. During the production, there can be material savings up to 90% but the energy savings can be better only for small series of production [1]

Interest in AM is growing since 1990s as ca be seen in fig. 1.1.

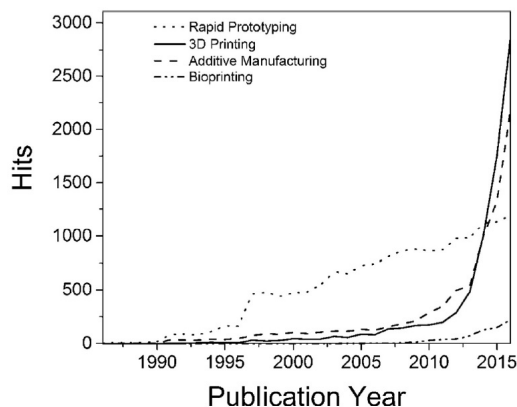


Figure 1.1.: Publications about rapid prototyping, 3d printing, AM and bio-printing according to amount of references per year [2].

1.1. Direct Energy Deposition and Powder Bed Fusion

AM can be divided according to the supplied filament. Material in this thesis was produced from powder material by Direct Energy Deposition (DED) method. There are various techniques using powders as a source material. There is an overview of the most common ones in the table 1.1.

Direct Energy Deposition (DED)	Powder Bed Fusion (PBF)
Laser based DED	Direct Metal Laser Sintering
Arc Directed Energy Deposition	Selective Laser Melting
Electron Beam Directed Energy Deposition (EB-DED)	Electron Beam Melting
	Selective Laser Sintering

Table 1.1.: Main types of Additive Manufacturing techniques incorporating powder source material.

1.1.1. Powder Bed Fusion

Laser or electron beam is used during Powder Bed Fusion (PBF). This beam melts powder and fuses material together. After creating of one layer, it is necessary to spread new layer of material and fuse this layer again together. Typical thickness of one layer is between 25 to 100 μm . New layer of powder is deposited by roller or blade and the powder is supplied via cartridge or hopper. Some materials or techniques require vacuum. Main advantages compared to DED is lower machine cost, wide material choice and in some cases possibility of recycling the powder. Disadvantages are longer printing time, higher post processing requirements and higher need of source powder.

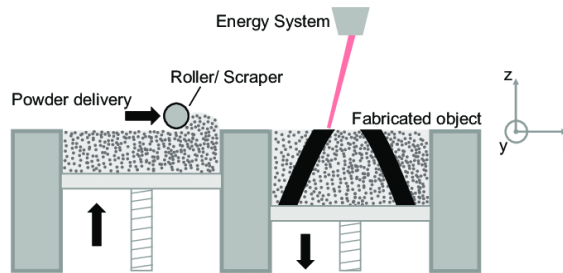


Figure 1.2.: Powder bed manufacturing process [3].

1.1.2. Direct Energy Deposition

Compared to PBF, DED uses different strategy to supply the source material. In this case the material is simultaneously supplied by nozzles directly to the melted pool and is melted by plasma arc, electron beam or laser. Samples investigated in this work were produced by DED and the source material was a powder.

The system for supplying the powder is composed of specially designed feeder that brings the powder to the nozzles. High energy beam is placed in the center of the system between the nozzles and is focused by a set of lenses on to the surface of the fabricated object. Motion of the lens and the powder nozzles in the Z direction guides and changes the focus of the beam on the surface of the product but the lens and nozzles can travel also in the X-Z direction. Fabricated object on the machine table can be in some applications moved in X-Y direction and tilted allowing 5-axes orientation. This helps to create required geometry of the weld cross-section. Each layer is placed on top or next to previous layer and this system creates final 3D product. Multi-axis tables and laser heads and continuous supply of the powder allows DED to create products with complicated geometries and very good dimensional accuracy. DED can be also used for repairs or refurbishments of damaged or worn out parts, and for coating corrosion resistance layers on to other products.

DED technology usually uses laser beam as a source of energy. In this case shielding gases like argon, nitrogen or helium are mostly used. There are two options of feeding the material. One is powder blown (see fig. 1.3) and the other one is wire feed. Samples in this thesis were created by powder

blown technology.

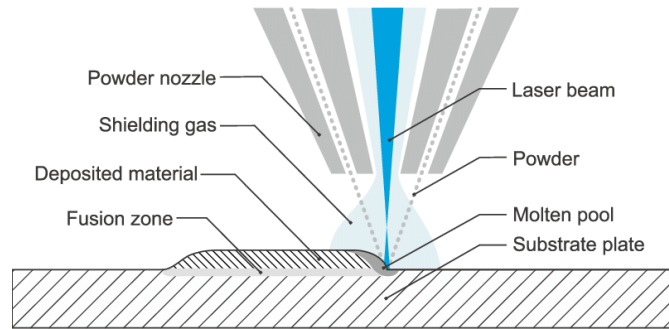


Figure 1.3.: DED manufacturing process [4].

Important part of the printing machine are high speed feedback sensors controlling the deposition process and sending real time data into the main computer. They are gathering information about the layer that is currently printed. The main computer can optimize the printing parameters according to this information, so the dimension accuracy and material integrity is kept. Powder used in DED is usually with grain diameter $d = 45 - 150 \mu\text{m}$. Advantages of DED compared to PBF are [5]:

- higher printing speed
- printing of heterogeneous materials
- combination of powders - creating different material than was the original powder
- coating of existing products
- less material waste
- Easy to refill existing material
- less post processing

Disadvantages of DED compared to PBF are

- dimension accuracy
- printing of porous structures is not possible
- At 3 axis system max overhang over 5° is not possible

1.2. Parameters of 3D printing

There are multiple parameters affecting the quality of the final print. Those with highest impact are mentioned in this chapter.

1.2.1. Laser power

Power of the laser is affecting the final shape of the melt pool which is described by the height and width of the melt pool. For lower power the powder can be melted only partially and the height and width of the melt pool can be not sufficient. This can result in small overlay between each layer and the resulting height of the layer in the Z axes could be too small or the surface can be collapsed. Further

the connection between the layers can be worse and the layer can later separate from the sub-layer. In the opposite case, when the power is too high, the height of the layer can exceed requested size. In extreme case this can lead to collision between nozzles and deposited material, because for each layer the nozzle is moving in Z direction only by predefined distance.

1.2.2. Print speed

Print speed is connected with the amount of energy invested into the material and will have effect on the melt pool dimension. Between the melted melt-pool and base material is high temperature gradient and surface tension. If the print speed is low, a lot of energy is added to the melt-pool, consequently, the temperature gradient and the surface tension will decrease during the transfer of the heat between melt pool and the surrounding environment. But the resulting surface of the melt-pool will be uneven and also local solidification can lead to cracks. In the opposite case, when the speed is too high, insufficient amount of energy is transferred into the material which can lead to worse adhesion between melt-pool and sub-layer. Other result of high speed can be insufficient melting of powder resulting in higher porosity.

1.2.3. Scanning strategy

Printing strategy (scanning patterns) can affect porosity, roughness of the surface, micro structure and mainly heat transferred into the previously deposited material. Main printing strategies are ZigZag, Parallel or Spiral (see fig. 1.4). For each type it can be further decided if also a contour will be used. Contour is a path bounding given layer which is then filled by some of the printing strategies mentioned above. Amount of contours depends on the required shape of the resulting edge.

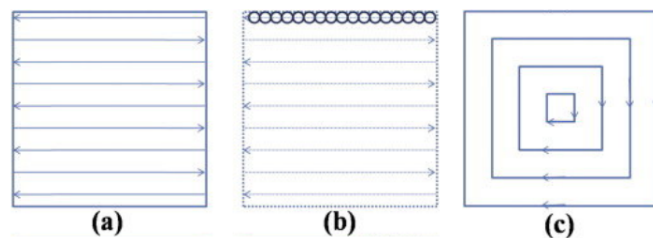


Figure 1.4.: Three main scanning strategies: a) Parallel, b) ZigZag, c) Spiral [6].

1.2.4. Layer height and Track width

Height of the layers in the Z direction is dependent on the optical system of the laser beam. Today, machines equipped with adjustable optics are available which allows to change the laser beam diameter during the printing. This will then affect the height of the layer. That in turn can affect resulting strength, roughness, micro-structure or resulting printing time. Distance between each track - track width - is smaller than laser beam diameter and should be around $2/3$ of laser beam diameter. For example for laser beam diameter 0.8 mm, the track width would be 0.5mm. This distance effects porosity, mechanical properties and resulting size in Z direction.

1.2.5. Special parameters of 3D print by DED

During the deposition of the material, it is crucial to keep the laser beam focused to the same spot where the powder injection takes place and also to keep it in the axis of the scanning direction. One

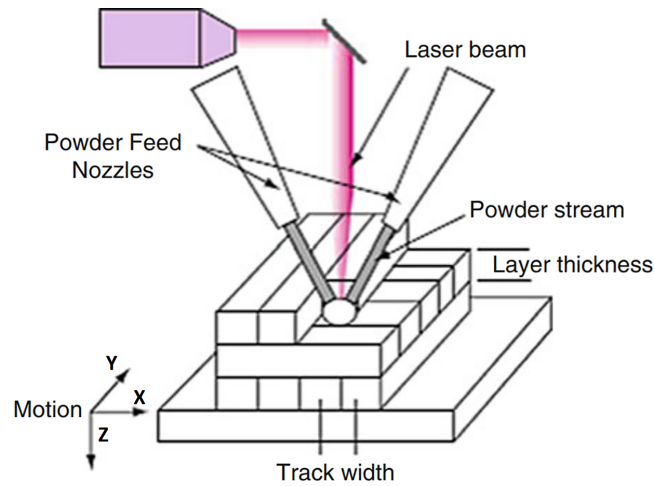


Figure 1.5.: Description of the printed layers [8].

of the reasons for that is the melt pool overlap. If the melt pools from neighboring tracks will not be in designed distance, risk of creating pores will increase. Only part of the weeded powder is in that case melted, rest of the powder will stick on the melted material. Another layer will cover this area and that will create pores [7].

1.2.6. Defects in DED

Even though the process of deposition is fully automatic, some defects may appear. These defects, like porosity, cracks or in-homogeneity, change the mechanical properties of the material and are undesirable.

Cracks

Most common reason for crack creation are poorly chosen printing parameters or the printing (deposition) process distribution without proper correction of the printing parameters [36]. Also when the base material for the printing has significantly different thermal expansion coefficient, the cracks may appear between these two materials. Cracks in the material then decrease the integrity and strength.

Porosity

Porosity (size and amount) can affect significantly the mechanical properties of the final product. We have 2 main types of porosity: inter-layer and intra-layer porosity. Inter-layer porosity is created when the ratio between laser power to scanning speed is too low. Then there is a chance that not all the filler material will be melted and that will create un-melted regions [39] which are usually located between the tracks. Size of the pores is usually larger and the shape is irregular.

Intra-layer porosity is connected with the shielding gas. During the deposition process some gas can be trapped inside the material and after the solidification a pore at that place can be found. These pores can be found anywhere in the material and are of the circular shape.

1.3. Aluminium bronze

Aluminium bronzes or sometimes also Aluminium coppers are alloys of copper with 5-12wt% of Al. Other alloying elements can be iron, nickel and manganese. According to chemical composition aluminium bronzes can be divided to “binary” (i.e. alloys of copper and aluminium without any additional

alloying), “ternary” (with two alloying elements) or “complex” (with more alloying elements), see table 1.2. Aluminium bronzes are used for their good mechanical properties, high wear and corrosion resistance, high impact resistance, good machinability and weldability and also resistance against cavitation. Compared to brasses or tin, aluminium bronzes have better corrosion resistance due to protective Al_2O_3 . Aluminium bronzes can also offer decent stability up to temperatures around 400 °[12], [13], [32].

Classification	Chemical content
Binary	CuAl
Ternary	CuAl + Fe, Ni, Mn, Si, Be, Sn, Co
Complex	CuAlFeNi, CuMnAlFeNi

Table 1.2.: Classification of Aluminium bronzes according to [32].

1.3.1. Copper

Copper was most probably one of the first metals used by humans and nowadays is the third most used metal. In general, the main properties why copper is so widely used are high electrical and thermal conductivity, good corrosion resistance and also good formability. Copper is non-polymorphic and creates crystal in Face-centered cubic system (FCC). Specific weight of copper is 8930 kg/m^3 , modulus of elasticity is 128 GPa, melting point is 1083°C , the thermal conductivity is $\lambda = 397 \text{ Wm.K}$ and electrical conductivity is $58.1 \times 10^6 \text{ S/m}$ [9].

1.3.2. Aluminium

Aluminium is the second most used metal after iron. It is widely used as pure aluminium or in alloys. It can be formed, cast, melted and machined. It has good electrical and thermal conductivity. Specific weight of aluminium is 2700 kg/m^3 . It has very good corrosive resistance, aluminium creates protective oxide coating, that can prevent the material from most types of corrosion. Other advantages are aluminium’s strength at low temperatures, and that it is impermeable, odorless, non-magnetic, non-toxic, and ductile. Melting point is 660.3°C , thermal conductivity is $\lambda = 205 \text{ Wm.K}$, modulus of elasticity is 69 GPa [10]. Aluminium creates FCC crystal structure. Aluminium bronze usually contents 5-13wt% of aluminium and aluminium is the main strengthening element. If the weight content is 13wt% then the hardness is highest but the ductility is reduced to 1%. As an alloy in Aluminium bronze, it can improve mechanical, tribological and corrosion properties [32]. It is important to control the amount of Al in the product, slight change of about 0.1wt% can affect the resulting mechanical properties.

From the start of the research of the binary alloys the results show appearance of participates and martensitic, ordering reactions. Micro-structure of AlCu is complex and during the time more types of phase diagram were produced. Nowadays, the one from Murray [33] is widely used (shown in the fig. 1.6). But it is still developing and some of its parts are improved and specified.

1.3.3. Iron

Iron is the most used metal and is used in wide ranges of applications. With increasing temperature iron will undertake two allotropic transformations and one change in magnetic properties. At room temperature iron has BCC lattice and a lattice constant of $a = 2.87\text{\AA}$. At 760° ferromagnetic iron α becomes paramagnetic and is called β . At 912° β iron with BCC lattice is transferred into the γ iron

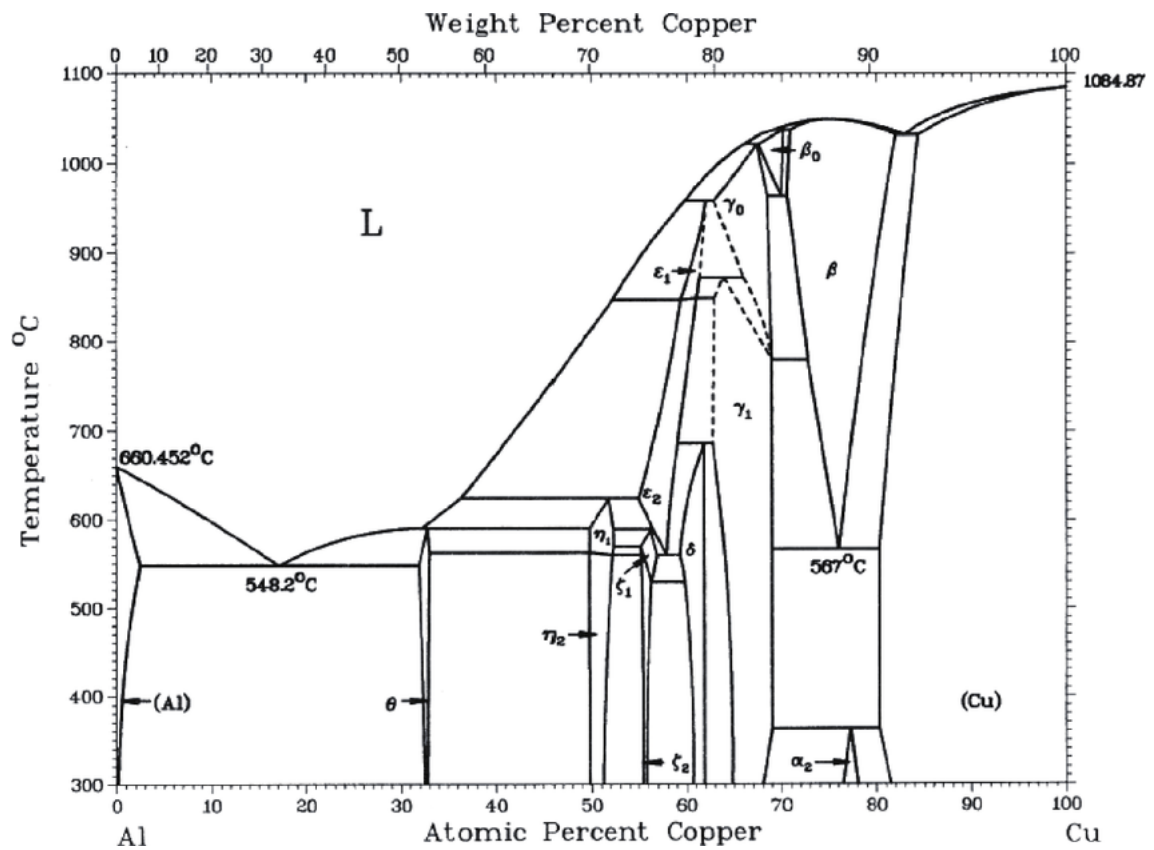


Figure 1.6.: Phase diagram for CuAl system. For purpose of this work the part around 20at% (9.42wt%) of Al is important [33].

with FCC lattice. Another allotropic transformation will happen at 1394° when γ iron converts to δ iron with BCC lattice. From this temperature till the melt point at 1539° the lattice structure is stable (see fig. 1.7). Specific weight of iron at room temperature is 7874 kg/m^3 [11]. In the aluminium bronze the iron slightly modifies original Al-Cu phase diagram. Iron helps to refine the grains.

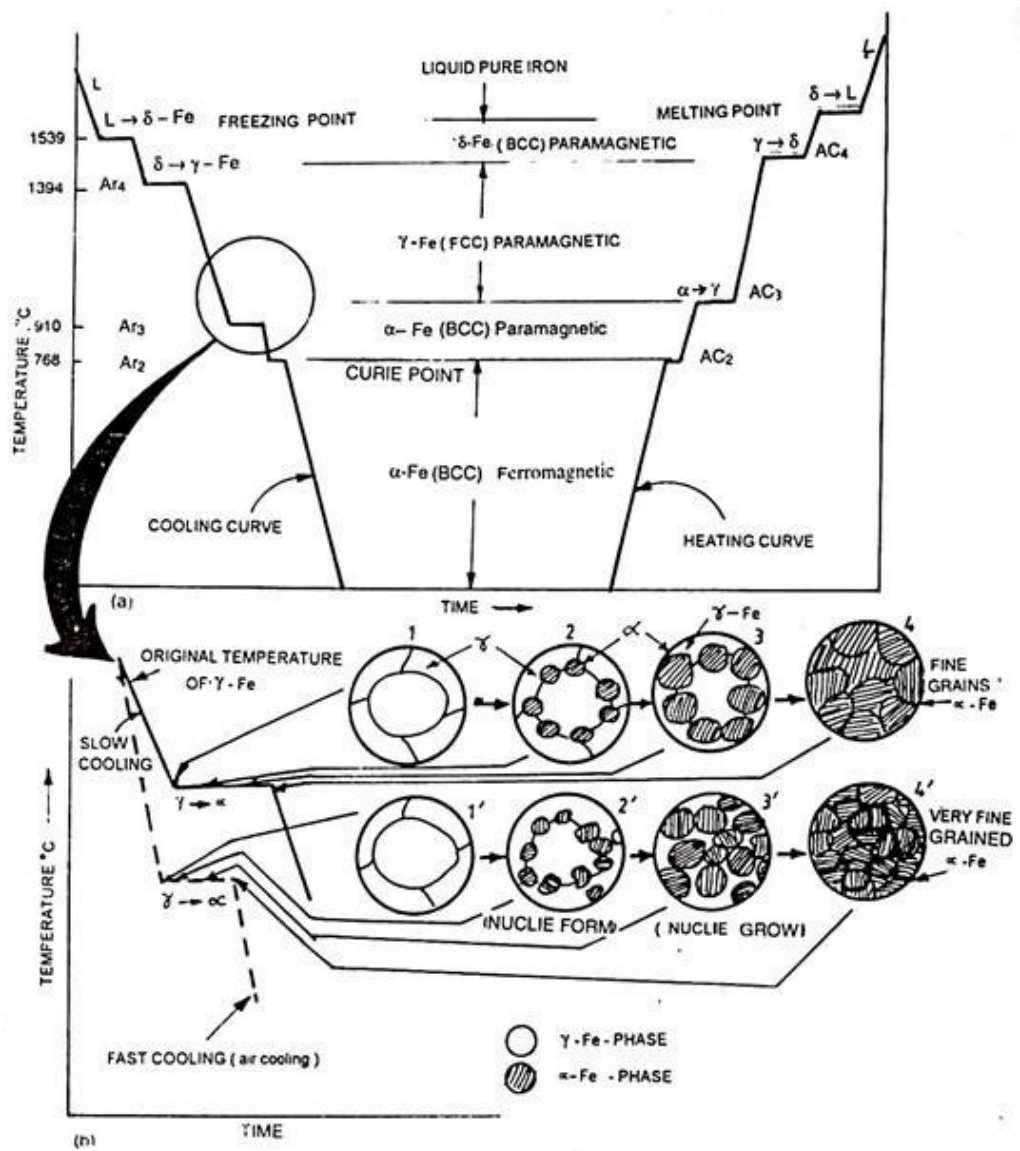


Figure 1.7.: a) heating and cooling curves of iron b) phase transitions [11].

1.4. Micro-structure of Aluminium bronze

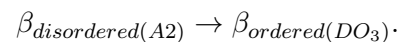
If the aluminium content is below 8 to 9wt%, then aluminium dissolves in copper and the resulting structure after cooling consists only from the α phase. If the aluminium content is higher (between 9 - 15wt%), then second phase known as β is created. This β phase is present only at higher temperatures and is stronger and harder. If the material is then slowly cooled below 565°C, then the β phase will change into finely divided structure (eutectoid). This new structure will consist of lamellar eutectoid α and γ_2 or sometimes also called γ' .

1.4.1. Alpha [α] phase

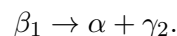
Alloys containing smaller amounts of aluminium (typically less than 6-8wt%) will solidify as a single α phase alloys with one homogeneous (Cu) phase [32]. That will cause the material to be of low hardness and high ductility. Based on the cooling rates alloys with Al content above 8wt% will give α and some other phases like β Cu_3Al . Alpha phase is white etching in the figures and the lattice parameter is 3.64Å- that differs very slightly from copper [41].

1.4.2. Beta [β] phase

Alloys with more than 9wt% of aluminium will solidify as β . From the phase diagram for binary Al-Cu system on fig. 1.8 it can be seen that when the temperature falls under 910°C, β will start to deposit from the α . The more the temperature lowers the more disordered β phase we get and it will start to undergo ordering reaction,



At this stage the structure looks like Widmanstatten structure comparable to that found in 60/40 brass [14]. It is a Cu_3Al compound with a wide solubility range [32]. Once the temperature reaches 565°C, eutectoidal decomposition of remaining β will happen,



But the β phase can be present even at lower temperatures, if the cooling rates are fast enough. In case of fast cooling rate the ordering reaction will precede the martensitic transformation [32], which leads to formation of metastable phases. There will be β' present below 565°C and it would transform into a “hard acicular martensitic form by a process not requiring diffusion” [14]. For higher Al contents (more than 12wt%) two ordered martensitic phases γ' and β_1' are present.

Only at slow cooling rates entire β can decompose. Transformation into Cu_9Al_4 (γ_2) will happen at first. This leads to the decrease of Al content in the matrix. When the Al content decrease below 10wt% than the α phase will start to form. This reaction requires time to be completed [32]. β phase forms BCC lattice. Strength of the β phase alloy is higher than for α phase alloy but the ductility at room temperature is lower.

1.4.3. alpha + gamma₂ [$\alpha + \gamma_2$] phase

This phase is created after slow cooling from higher temperatures and starts to occur below 565°C. Aluminium content of γ_2 phase is higher than the one in β phase. Corrosion properties are similar to that of the β in brasses. If γ_2 is isolated, then the risk of corrosion is not severe, but if the γ_2 creates a continuous network, the risk of the corrosion and penetration through the material increases. So the

creation of γ_2 phase can significantly affect the corrosion resistance of the material and the corrosion can penetrate into the body of the material.

Addition of Fe helps to refine the structure and should restrict creation of the γ_2 phase. Also the amount of aluminium can help to prevent the γ_2 phase. According to [15], content below 9.1wt% should restrict formation of continuous network of γ_2 phase. Also the cooling rate affects the size of γ_2 phase but according to [15] even the slowest cooling rates for Al 8.7-9.1wt% will not create continuous network and the gamma phase is then discontinuous.

1.4.4. Kappa [κ] phase

Addition of small soluble amount of Fe into the Al-Cu does not affect the matrix but leads to formation of the inter-metallic Fe_3Al κ precipitates. According to Al and Fe content and cooling rates it can have FCC or BCC lattice. For example for $\text{Fe}_4\text{Cu}_8\text{Al}_9$ that is slowly cooled, Fe forms a BCC phase with 0 to 5%Cu, up to 13.5%Al and Fe which is very well crystallized [41]. κ phase could be found in alpha and beta phase and precipitates in large globules where some have diameter μm . Addition of 2%wt Fe and formation of κ phase improves the tensile strength and the hardness increases [32], but it also reduces the the percentage elongation.

1.4.5. Iron

As mentioned above, one of the ways how to prevent creation of γ_2 phase is to add Iron and or Nickel. Besides this, iron refines the structure. Publications [15] [32] usually say that 2wt% of iron should be sufficient. Iron particles precipitate through both phases α and β . But the temperature when the precipitation starts varies according to the amount of aluminium present [14]. For smaller wt% of aluminium and for α alloys, the iron solutes when the temperature gets below 1000°C. For alloys with higher amount of aluminium, the iron will start to precipitate at around 850°C. The precipitates of iron can be observed evenly distributed through the structure. Solubility limit of Fe in the Al bronze is around 3.5wt% and till this limit all Fe is usually retained as a solid solution but some Fe rich particles (BCC αFe) can be observed [32].

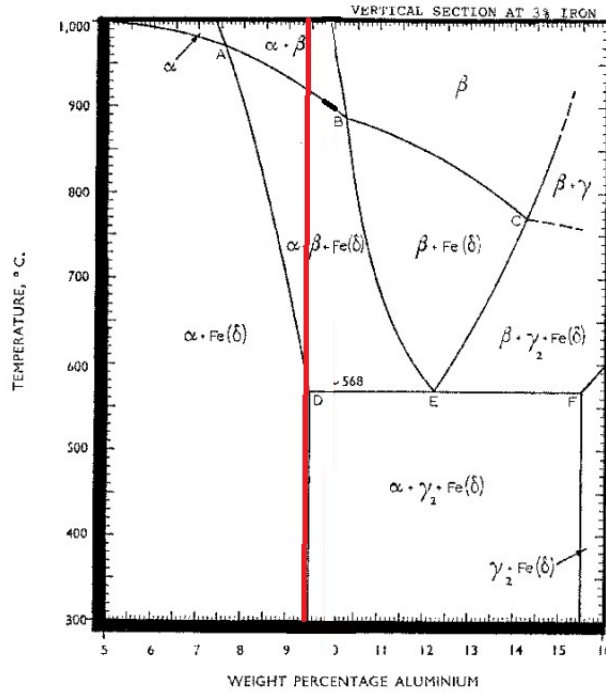
Iron also improves the corrosion resistance, but it must be solid solution and should not precipitate as pure Fe [32].

1.4.6. Dislocations

Dislocations are included in the crystal when some mechanical force is applied like during the solidification or during a plastic deformation. It is a linear crystallographic defect. We have two basic types of mobile dislocations - edge and screw (fig. 1.10). Combination of these two is called mixed dislocation. The amount and the orientation or arrangement affects material properties. Dislocation starts and ends on the crystal wall or is connected to itself and creates a loop.

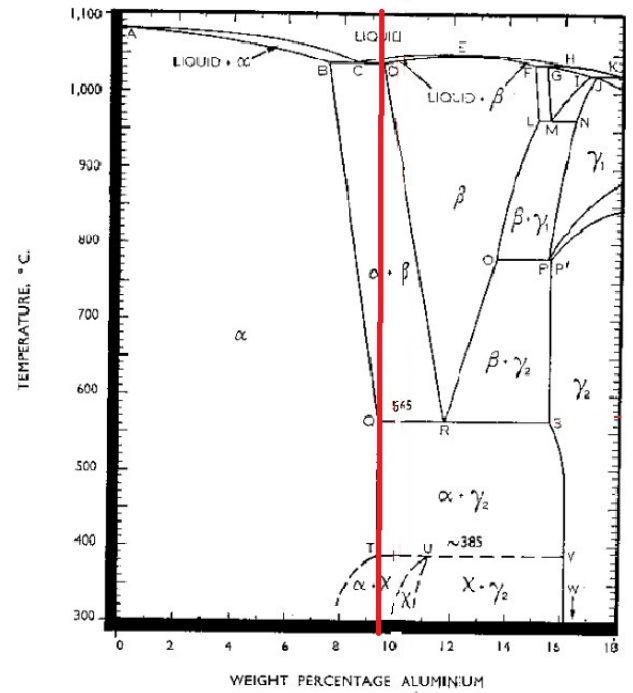
Edge dislocation with the Burgers vector being perpendicular to the dislocation line is a dislocation where half plane of atoms is added in between an existing crystal. Burgers vector together with the dislocation line creates (defines) the slip plane. At screw dislocation the Burgers vector is parallel to the dislocation line and there is a lot of slip planes in which the dislocation can move. Movement of the edge dislocation is energy efficient. Oscillation in the lattice disrupts the bond around the dislocation and it will shift by one inter-atomic distance [38].

Copper-Aluminium-Iron



Point	A	B	C	D	E	F
°C	970	885	770	-568	-568	-568
Al, %	7.6	10.3	~14.3	9.5	12.3	15.5

Copper-Aluminium



Point	A	B	C	D	E	F	G	H
°C	1083	1037	1037	1037	1048	1036	1036	1036
Al, %	0	7.5	8.5	9.5	12.4	14.95	15.25	16
Point	I	J	K	L	M	N	O	P, P'
°C	1022	1022	1022	963	963	963	780	780
Al, %	16.9	17.1	18	15.1	15.45	16.40	13.6	~15.6
Point	Q	R	S	T	U	V	W	
°C	565	565	565	~385	~385	~385	0	
Al, %	9.4	11.8	15.6	9.4	<11.3	16.2	16.2	

Figure 1.8.: Left phase diagram is for Copper Aluminium Iron (3wt%) and right phase diagram is for Copper Aluminium [14]. Red lines represent Aluminium content of the tested samples.

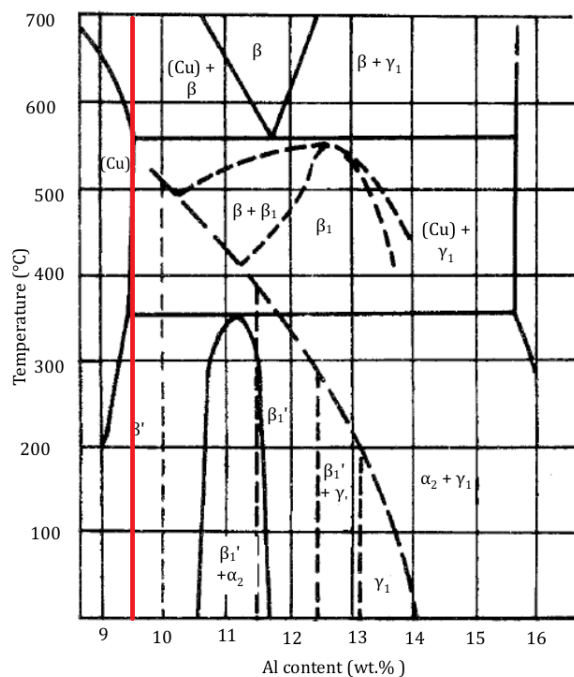


Figure 1.9.: Section of the Cu-Al phase diagram [32], red line depicts Al content for the tested samples.

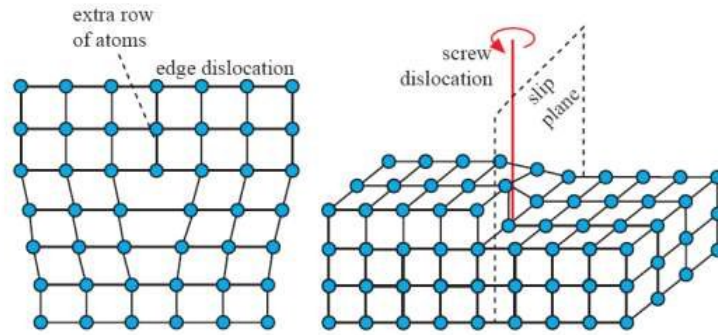


Figure 1.10.: Schematic diagrams of A) an edge and B) screw dislocation in an atomic lattice [37].

1.5. Hardness testing

Hardness testing is cheap and fast method, that can give us good overview about one of the basic material property. There are various test machines with different inventors. In my case Vickers hardness test was used. The test is usually carried out multiple times to get overview about grater part of the sample surface. Sample is placed into the machine. Indenter then presses against the sample with required force for 10-15s. Size of the imprint is then measured and the result gives us resistance against deformation, see fig. 1.11. In case of Vickers test, the indenter has shape of a pyramid. Load is adjusted according to material and can be between 1 - 120kg. All the tests were carried out according to EN ISO 6507-1:2018 standard [30].

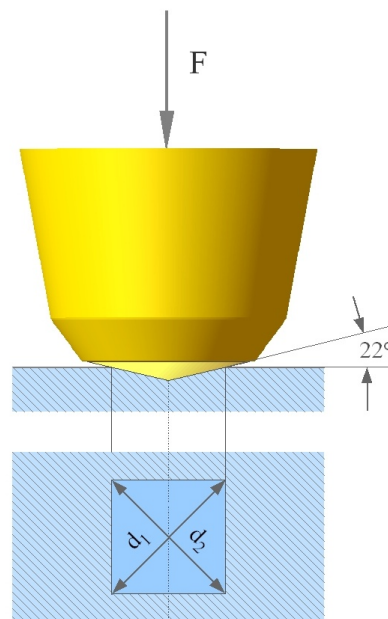


Figure 1.11.: Schematic drawing of Vickers hardness test indenter [29].

1.6. Microscope

Various types of microscopes were used. In the start of the work light microscope (LM) was mainly used to quickly investigate the structure of the material. Later in the research, also the transmission electron microscope (TEM) and scanning electron microscope (SEM) were used. To investigate the phases in the material, also X-ray diffraction was used.

1.6.1. Light microscope

During the research Olympus GX53 inverted microscope was used (see fig. 1.12). LM is used for observing objects not visible by naked eye, sometimes also the term “optical microscope” is used. Magnification of the LM is from 5x to 100x and we can observe objects from 0.2mm to $0.2\mu\text{m}$. Some microscopes can also use special sources of light to improve the observation. For example, circular LED illumination for dark field to reduce the halation improves the visualization of surface texture [17]. Optical system of LM composes of 3 main parts - objective lens, ocular lens and the condenser.

Objective lens

Most important part of the LM is the objective lens. It usually consists of multiple lenses. Investigated object must be placed in the distance between f and $2f$ so we get real, enlarged and overturned image. Focal length is very short (in millimeters). Objective lens determines the magnification and the quality of the resulting picture. To get higher magnification, we have to turn the revolver head and change the objective lenses. These lenses are usually colored for faster orientation [16].

Condenser

In the inverted microscope is condenser located below the stage and above the light source.



Figure 1.12.: Olympus GX53 used during the research. Sample is placed on top deck and the objective lens is located below the sample. Condenser is improving the illumination of the specimen by gathering from the light source and pointing it to the sample [17].

1.6.2. Electron microscope

Electron microscope (EM) helps us to investigate objects up to the size of nanometers. Beam of electrons is used in EM, compared to LM where the beam of photons passing through the lenses is used. The electrons in EM are passing through the system of lenses as well, but in LM glass lenses are used whereas in EM electromagnetic lenses are used. Electromagnetic lenses are coils creating magnetic field with required shape. Using electron beam instead of photon beam increases resolution

of the microscope. Resolution of the microscope can be calculated as:

$$\text{resolution} = \frac{0.61\lambda}{\eta \sin \alpha}$$

where λ is wavelength of the beam, $\eta \sin \alpha$ is the objective numerical aperture [20]. The value calculated in this way is only theoretical, and in real life the magnification is smaller due to additional errors caused by limitations in the construction of the microscope. It is also obvious from the formula above that the resolution of EM is greater than for the LM and the different values can be compared in table 1.3.

Parameter	Light microscope	Scanning el. microscope	Transmission el. microscope
Magnification	(4 - 1000)×	(10- 2×10 ⁶)×	(100 - 5×10 ⁷)×
Depth of field	15.5mm - 0.19mm	4mm - 0.4mm	0.00001mm
Resolution	0.2mm	1 nm - 20 nm	0.050 nm
Sample thickness	Any	Any	<150 nm
Accelerating voltage	-	5 - 20kV	100 - 300kV

Table 1.3.: Main differences between light microscope, scanning electron microscope and transmission electron microscope [18], [19].

Resolution of EM can be adjusted by accelerating voltage U . That is voltage between the cathode (source of electrons) and anode. Due to the accelerating voltage, an electron with charge $e(1.60210^{-19}C)$ and mass $m(9.10910^{-31}kg)$ will gain kinetic energy E_k that is :

$$E_k = eU = \frac{1}{2}mv^2.$$

We can consider electron as a mass particle but also as a plane monochromatic wave with wavelength λ :

$$\lambda = \frac{h}{p} = \frac{h}{mv}$$

where h is the Planck constant ($6.62610^{-34}Js$) and p is electron momentum. Combining the above equations, a relationship between acceleration voltage and wavelength of electron is obtained:

$$eU = \frac{h^2}{2m\lambda^2}.$$

Source of the electrons in EM is an electron gun. Efficiency of electron emissions can be increased by proper shape of the cathode. Electron guns can be divided according to energy supply to the emitted electrons:

- Thermionic - Cathode is heated and so the inner energy is increased. When the limit temperature is exceeded, the electrons are emitted from the surface of the heated cathode. Materials used for this type of cathode are tungsten (lifetime approximately 100 hours), lanthanum hexaboride crystal (lifetime approximately 250 hours). Advantage is a stable electric current as large as $1\mu A$.
- Field emission - Tip of the cathode has very small curvature of about 100nm. Opposite to the cathode an electrode with high positive current is located. Around the emitter tip of the cathode strong electric field is created which is able to emit the electrons from the surface. This procedure requires high vacuum. Material used is tungsten with unlimited life time.

Interaction between electrons and sample

When the beam hits the sample, scattering will occur. In case of electron microscopy we get two types of scattering - elastic and inelastic. This results in wide spectra of signals from which we can get multiple information about the sample. Different electron-matter interactions can be seen in the fig. 1.13.

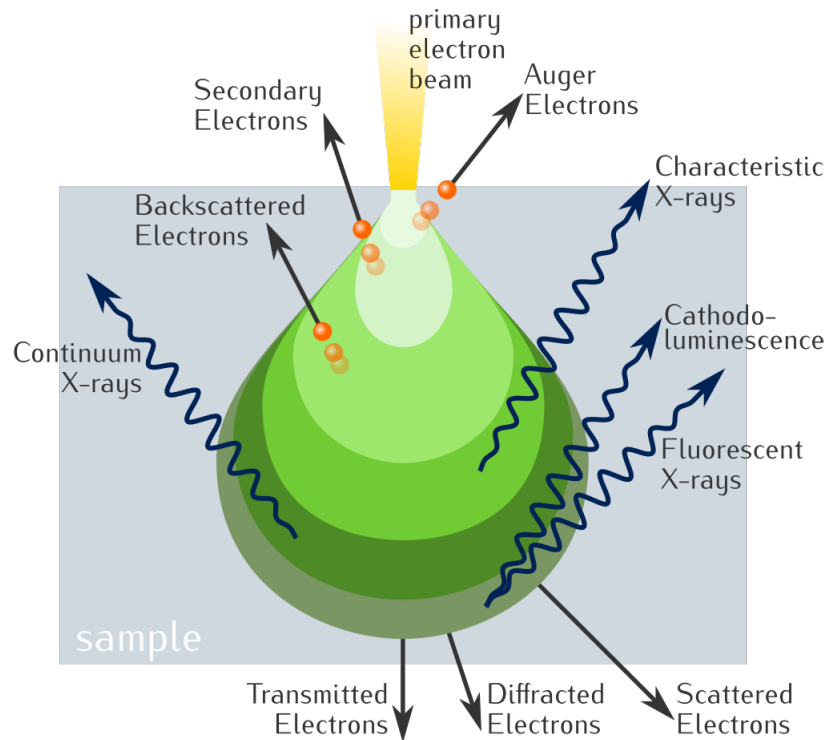


Figure 1.13.: Electron-matter interaction volume and types of signal generated [21].

There are two basic types of Electron microscopes - Scanning electron microscope (SEM) and Transmission electron microscope (TEM).

1.6.3. Scanning electron microscope

SEM is technically more complicated than TEM, therefore it was introduced later than TEM. Advantage of SEM is the procedure of sample preparation. Sample needs only to fit the chamber and the sample holder and is not required sample thickening to μm as for TEM. As can be seen in the fig. 1.14, we can get various signals about the sample. This information can be included in the amount of back scattered electrons or secondary electrons, in distribution of their energies, direction of the emission or combination of these factors. Back-scattered electrons (BSE) are result of the elastic scattering from the sample. Their energies are usually in the range $0.7\text{-}0.9 E_0$ (primary energy). BSE are from deeper parts of the sample and include information about composition of the sample [22], [23].

Secondary electrons (SE) are from the inelastic interaction at the surface or near-surface of the sample. They are used for the inspection of the topography of the surface. Secondary electrons have small kinetic energy in the range $0\text{-}50\text{eV}$, mostly $3\text{-}5\text{eV}$. An X-ray signal is also created in the sample which can be used for the chemical analysis of the sample.

Depth of interaction of the beam with the sample is dependent on the atomic number of the material the sample is made from - the smaller atomic number, the deeper electrons can get.

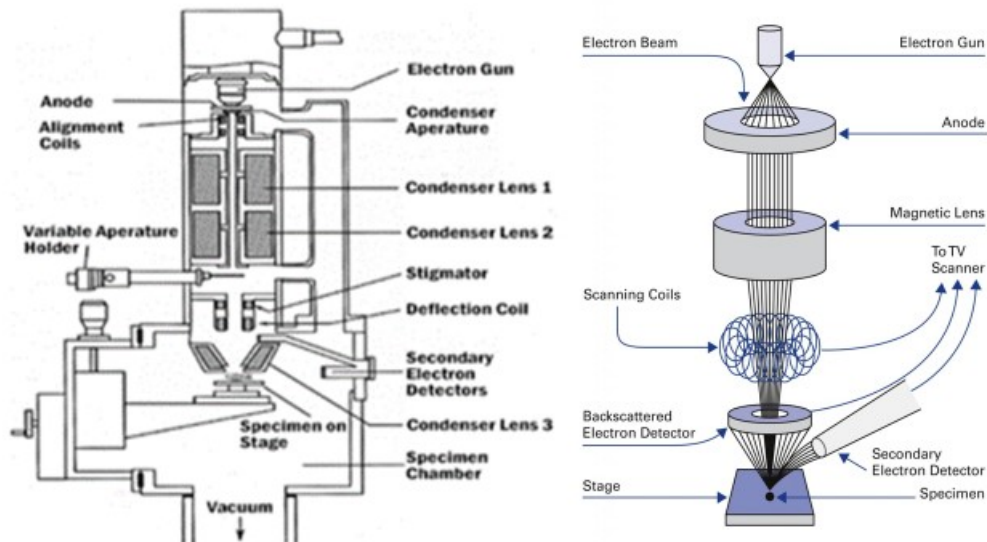


Figure 1.14.: SEM scheme [22].

1.6.4. Transmission electron microscope

TEM allows us to investigate micro-structure of materials from size of μm down to atomic level. TEM JEM-2100 with 200kV acceleration voltage used for the investigation is depicted in the fig. 1.15. In the main box the vacuum system and the electronics are located. The power box and high voltage tank are located separately. In the vertical tube, there is electron gun, electron accelerator, electromagnetic lenses and the fluorescent screen. For the process of sample investigation high vacuum is required, usually between 10^{-3} - 10^{-5}Pa . Highest vacuum is required around the electron gun and around the sample. Sample is located approximately in the middle of the tube [24].

Electron emission in our TEM is done by crystal of lanthanum hexaboride (LaB_6)[26]. Electron gun then produces a beam of electrons with the density around $10^{10}\text{Am}^{-2}\text{sr}^{-1}$. Another key part of the TEM is the objective lens. Best lenses for 200kV TEM have spherical aberration $C_s=0.5\text{ mm}$. This parameter together with (LaB_6) cathode allows us to get resolution around 0.19 nm. On the other hand the low coefficient of spherical aberration requires the lens to be placed close to the sample. Therefore the tilting angle is limited usually to $\pm 15^\circ$. But we mostly need to tilt the sample more, sometimes up to $\pm 60^\circ$. Therefore we use objective lenses with higher coefficient of spherical aberration.

Requirements on sample preparation for TEM are high. The thickness of the sample should be usually less than 100 nm. Then the electron beam can pass through the sample and the magnified image can be formed on the imaging device. Imaging device can be fluorescent screen, photographic film or scintillator. The image is formed when the beam of electrons is passing through the sample and the electrons are interacting with the atoms in the specimen. Electrons inside the sample can have elastic and inelastic interactions. Different signals are depicted in fig. 1.13.

During elastic scattering, the electrons interact with the electrostatic potential of the nucleus of an atom. During the interaction, momentum is changed which is always connected with a small change in energy. Because of the big weight difference between electron and atom, this energy change is negligible. During inelastic scattering, primary electrons are interacting with the electron shell. The primary electrons are losing some amount of energy, which is transferred to the electrons in the electron shell and excite them. Later deexcitation occurs and energy is released, which can be detected with appropriate detectors.

Crystalline material, when properly oriented, can experience electron diffraction on some crystal planes. If all the parts of the electron beam are parallel, then electrons diffracted on different parts of the crystal planes are also parallel. These resulting parallel beams are then focused by objective lens into the points in the back focal plane (objective diaphragm). In this way Fraunhofer diffraction pattern is created, which represents Fourier transform of the wavelengths of the wave leaving the sample. The diffraction pattern should be further indexed to get the final information about the crystal type. Directions and dislocation are determined by Burger's vector [24].

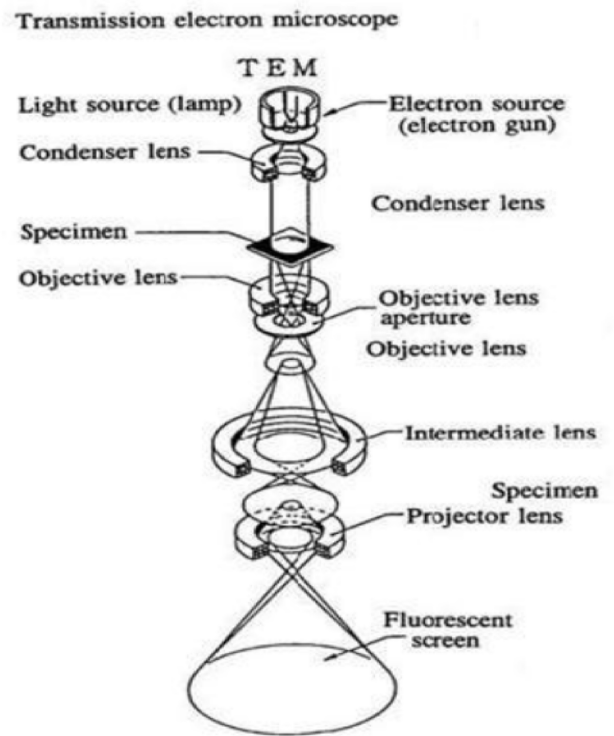


Figure 1.15.: TEM (JEM-2100) located at the University of Stavanger and the scheme of TEM [25].

1.6.5. X-ray Diffraction (XRD)

One of the usage of the XRD is to determine the crystallographic structure of the material. About 95% of all solids can be described as crystalline [27]. Interaction with matter creates multiple responses, as discussed before, but for XRD diffraction is the most important elastic scattering. Here the wavelength of incident and scattered electron beam is similar. Bragg's law can describe the general rule for interference of two beams - the path difference must be integer times the wavelength:

$$2d \sin \theta = n\lambda$$

where θ is the angle between the electron beam and the crystal plane, d is the distance between the crystal planes, n is an integer and λ is the wavelength.

The sample should be a polished solid or a milled powder. When placed into the machine, the X-ray source is moving in specific angle above the sample and on the opposite side with the same angle is located detector. Sample can be stationary or can rotate. Resulting diffraction patterns are used to identify the phases. Many diffraction patterns have been previously revealed and described and the one in [28] is similar to that calculated from our results.

1.6.6. Indexing of diffraction patterns from TEM and XRD results

Two main techniques how to describe the material phases were used - TEM and XRD. To compare their results for the d value, θ was calculated and the indexing was carried out. At first the Diffraction pattern (DP) from TEM was indexed and than the d value was used to find what peaks in XRD pattern belongs to which hkl values and phases.

- *.jpeg picture from TEM was scaled according to the scale bar

- Distance r between the spots was measured (preferably more spots with the same $\sqrt{h^2 + k^2 + l^2}$ to get average r)
- value was converted from inverse scale to get the d spacing ($1/r$)
- ratio of two d values is calculated and then compared with the table from [40] to find appropriate hkl ratio $\frac{d_2}{d_1} = \frac{\sqrt{h_1^2 + k_1^2 + l_1^2}}{\sqrt{h_2^2 + k_2^2 + l_2^2}}$
- lattice parameter a is calculated from the d value $a = d\sqrt{h^2 + k^2 + l^2}$
- θ is calculated from the d value and this result is compared with result from XRD using the formula $2d \sin \theta = \lambda$.

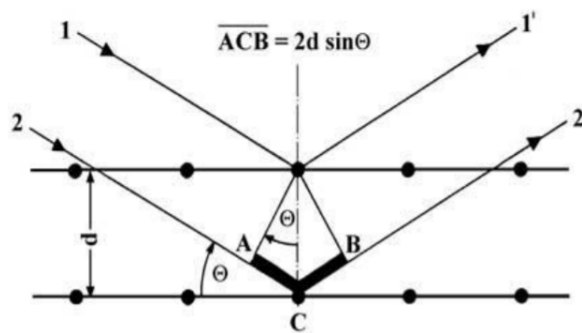


Figure 1.16.: Scheme of Bragg's diffraction condition - sum of length AC and CB is path difference between beams $1'$ and $2'$ diffracted from two neighboring atomic planes [27],[28]

2. Methodology

In order to properly understand the problem, available papers related to the topic were studied. Results from these papers were compared to the results obtained during examination of the 3D printed aluminium bronze. Most of the used materials described in the publications have slightly different chemical composition. Also the process of production of the final product was not exactly the same, yet it was still possible to compare the results. All the tests were carried out in the laboratories of the University of Stavanger except for SEM results from Oslo University. SEM, SEM and XRD analysis was done by lab engineers. All details about the experiments are included in this part of the thesis. It can be seen in the figures 2.1, that the samples were curved and bent, therefore it was decided to omit tests of mechanical properties except for the hardness test, because of the lack of samples according to standards.

2.1. Direct Energy Deposition - Sample properties

Material for the purpose of research was printed and delivered by Nordic Additive Manufacturing Raufoss, Norway (NAM). Company is producing marine propellers (see fig. 2.3) and the material delivered for the purpose of the research were parts of these propellers - see fig. 2.1. Size of the samples was from 5x2x3 cm to 25x4x15 cm. All the samples were printed on machine Trumpf True Laser cell 3000. Argon was used as a shield gas. This machine uses laser to melt the powder, which is blown into the melt pool from one nozzle. Thickness of each layer is 0.95mm for one type of samples or 1.5mm for another one. Thickness does not change within the printing. Samples have only one layer thickness. For the smaller thickness laser power 2200W is used. ZigZag scanning strategy with contour is used. Every second layer is turned by 90° - see fig. 2.4. Directions of scanning are called Transverse direction if it is along X-axis, Longitudinal direction along Y-axis, and the Build direction along Z-axis. Samples were cooled after printing in room temperature. No quenching or any other heat treatment was reported.

Powder supplier is Oerlikon metco and the product name is Metco 51NS. This powder is manufactured by gas atomization with density 3.9-4.3 g/cm³. Particle size distribution of the powder is -125 +45 μ m. According to the product list (see Appendix 1) the chemical composition of the powder is given by table 2.1.

Material	Value	Unit	Value	Unit
Cu	89.38	wt%	79.63	at%
Al	9.42	wt%	19.74	at%
Fe	1.1	wt%	1.10	at%
N	0.005	wt%	0.02	at%

Table 2.1.: Chemical composition of the powder Metco 51NS.



Figure 2.1.: Samples from Nordic Additive Manufacturing [21].

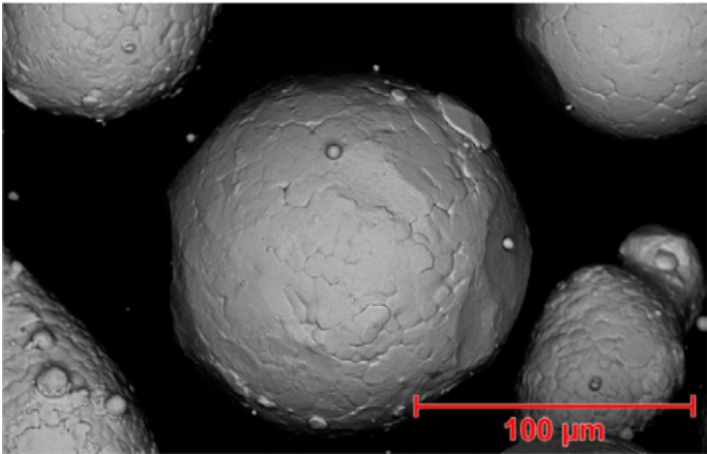


Figure 2.2.: SEM image of the Oerlikon powder Metco 51NS [31].



Figure 2.3.: Final product - marine propeller (Photo by: NAM)

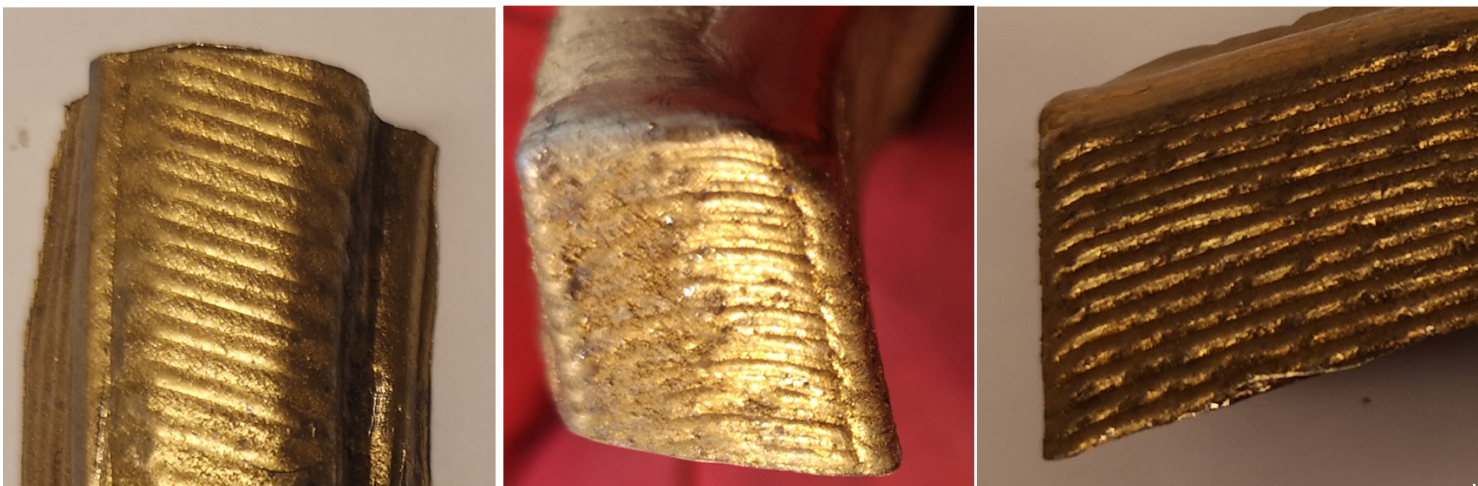
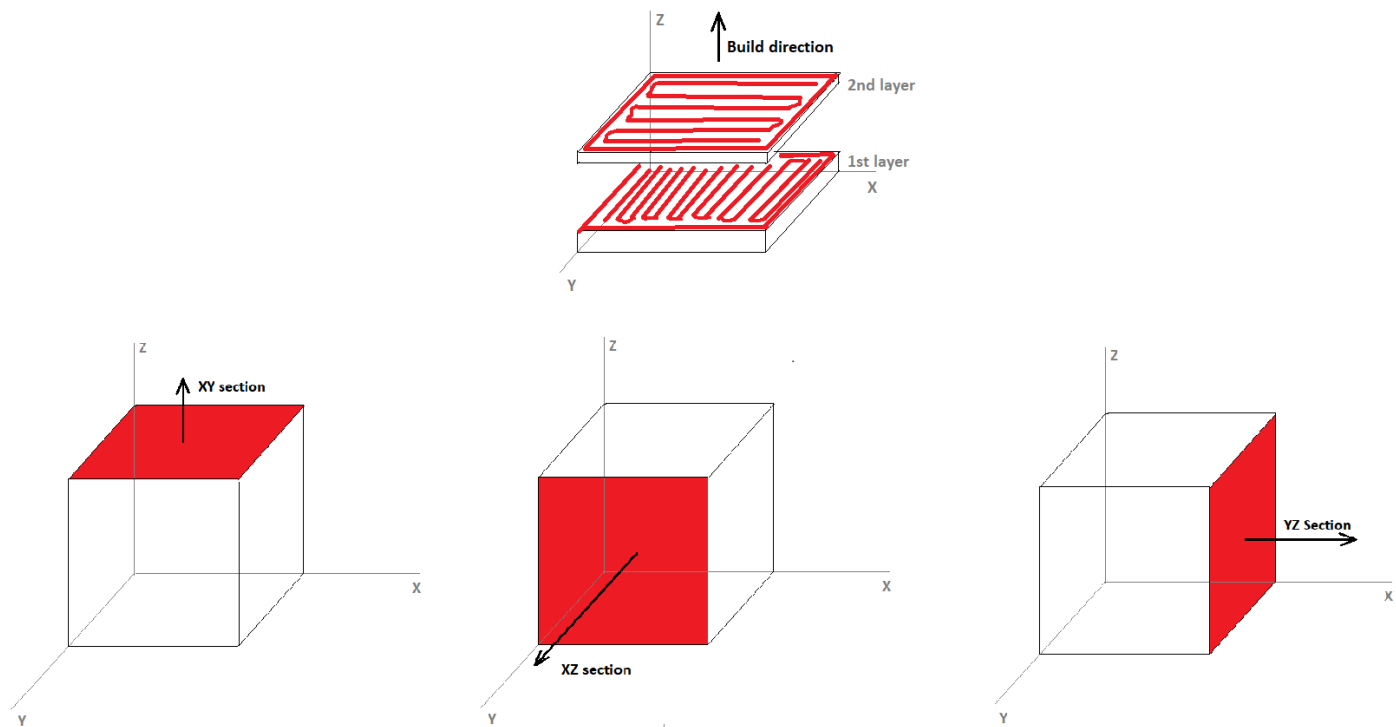


Figure 2.4.: Scanning method of the DED samples

2.2. Sample preparation

For the purpose of investigation of the material's micro-structure, it was necessary to prepare the samples. At first they were cut in all 3 sections XZ, XY and YZ. These surfaces were then polished and etched to obtain proper micro-structure. Hardness of the material is around 54 HV5, so few polishing procedures were tried, before obtaining the right one.

2.2.1. Cutting

The specimens were first cut on the band saw to get samples suitable for precise cutting. Then the samples were cut on Struers Discotom-10. This cutting machine is equipped with 2mm cut-off wheel and samples for LM, SEM and XRD were cut here. Samples for TEM were further cut by Struers Accutom-2 where it was possible to obtain samples with thickness around 1mm. Dimensions of the specimens for LM and SEM were about 3 x 3 cm.

2.2.2. Hot Mounting

To be able to polish the samples, it is first necessary hot-mount the samples. Struers CitoPress-30 was used to mount the specimens. Clarofast and Condofast hot mounting resins were used.

2.2.3. Grinding and polishing

Main aim was to create scratch-free and reflective surface. Tested material was softer, therefore it was necessary to keep the specimen and the grinding and polishing discs as clean as possible. It was found that the best method is the Struers method for Copper Bearing Alloys using DiaPro abrasives, see table 2.2. In the first three steps Silica Carbide (SiC) papers were used for polishing. In the last two steps polishing pads were used. For the second last step 3 μm diamond suspension was used and for the last step we used suspension consisting of 96% of Struers OPs suspension + 2% of ammonia (25%) + 2% of hydrogen peroxide (30%). Samples were cleaned in water and ultrasonic cleaner after each step.

Step	Grinding			Polishing	
	Plane grin.	Fine grin. 1	Fine grind. 2	Polishing	Oxide polish.
Surface	SiC foil 800	SiC foil 1200	SiC foil 4000	Md-Mol	MD-Chem
Abrasive type				DiaPro Mol R 3 μm	OP-S, 0.25 μm
Lubricant type	Water	Water	Water	Md-Mol	MD-Chem
Speed (rpm)	300	300	300	150	150
Force (N)/ 25	25	25	25	25	15
Time (sec)	60	60	60	240	60

Table 2.2.: Grinding and polishing procedure.

2.2.4. Sample preparation for TEM

First step in specimen preparation for TEM was cutting on Struers Accutom, where 1mm thick sample was cut. One side of the cut specimen was prepared as described in previous section and the other one was polished with SiC paper 2000. From this thin specimen were cut discs of diameter 3mm. Next step was electropolishing on Struers TenuPol-5. Sample was electro-polished from both sides simultaneously. Temperature during the polishing was -20°. Electrolyte was 4% perchloric acid (1066ml

of methanol + 44ml of perchloric acid (70%)) and various voltage was applied with various results (see table 2.3). Electropolishing was stopped automatically by an infrared detector, when the sample was perforated. Electropolishing time was in seconds to max 50 seconds. After the polishing the samples were immediately rinsed into the ethanol. Three fresh ethanol baths were applied fast one after another.

Voltage	Result
30V	small hole at the side
15V → 75V	no hole and after increasing voltage is the hole too big
12V	hole on the side
12V	hole in the middle - good for TEM

Table 2.3.: Different voltages during electropolishing for TEM.

2.2.5. Sample preparation for XRD and the test program

Specimens were cut using Struers Accutom machine and then polished on SiC paper, so that the height does not exceed the size of the holder and so that the surface is flat. One sample from each section was prepared (see fig. 3.2). Also coarse “powder” was prepared by three different methods. First try was to take the residual material after grinding. Material was full of water, so it was filtered through the filtration paper and then dried for 5 days. Second try was using a file and third method was powder which was left after cutting with saw (see fig.2.6). All the powders were further crushed or milled by hand, but this was not very efficient.

Samples were tested on Bruker D8 advance Eco A25 machine. Program duration for each sample was 50 minutes. Solid samples were rotating during the measurement and the powder samples were stable. Diffraction angle was from 0° to 90°.

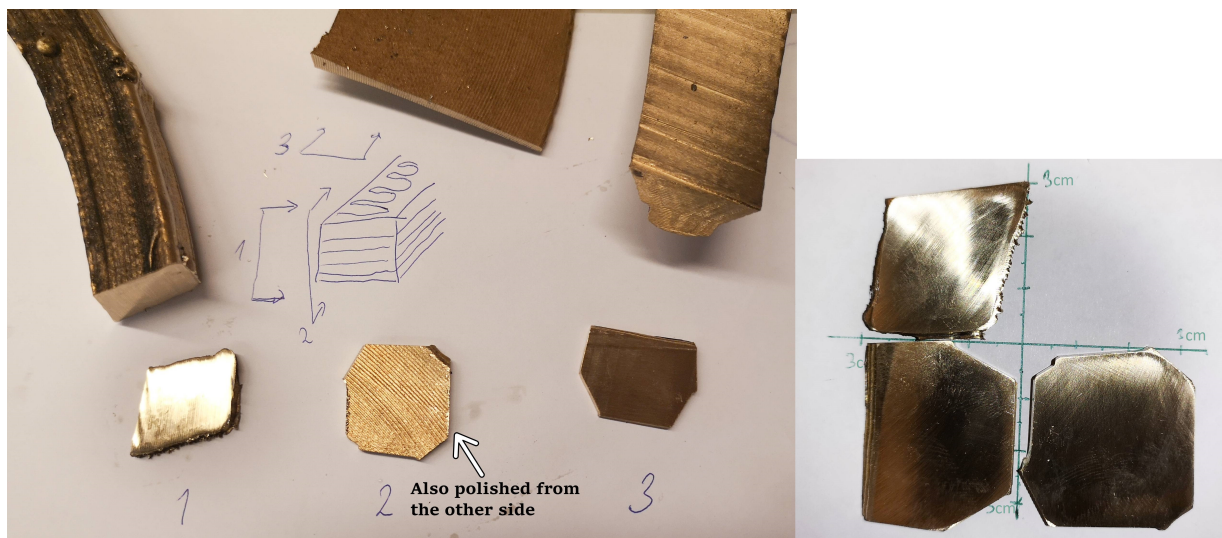


Figure 2.5.: Solid samples for XRD measurement - one from sample for each section - XZ, YZ and XY.

2.2.6. Sample preparation for Hardness testing

Three samples for each plane were prepared in the same way as the samples for SEM, so that the surface is free from anything that can influence the test results. They were cut, hot mounted, grinded, polished and oxygen polished. One sample from each section was prepared. Vickers hardness method was used with the loading of 5kg for 10s. Distance between the indents was 1 mm and the distance



Figure 2.6.: Powder preparation for XRD - uppermost picture is grinding and then filtering of the “powder”. Middle picture is from saw cutting and the lowest picture is preparation using the file.

from the edge was more than 10mm. 10 indents were made on each section. Approximate location of the indents can be seen on fig. 2.7.

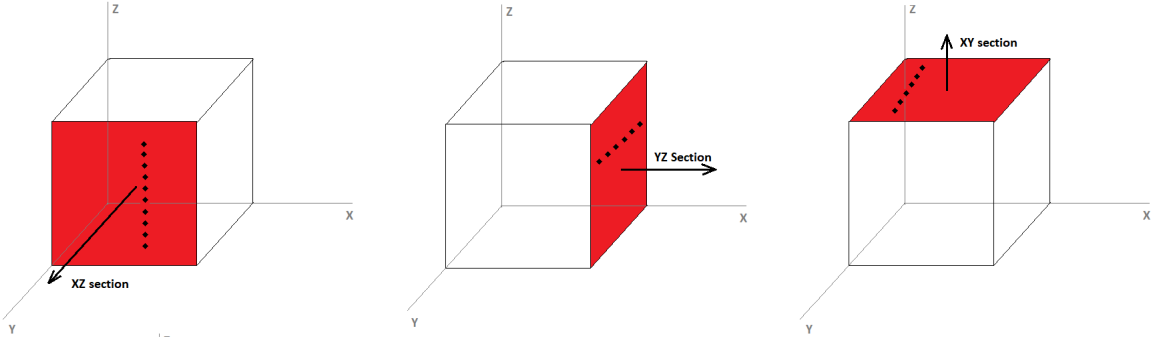


Figure 2.7.: Schematic picture of indents on 3 different sections.

3. Results

In this chapter results of the tests and investigations carried on the Aluminium-bronze samples are presented. Test and investigations were done on optical microscope, SEM, TEM, hardness testing and XRD.

3.1. Hardness test

Mean hardness for the section XZ is 51.6 HV5 and standard deviation is 0.84.

Mean hardness for the section XY is 52.3 HV5 and standard deviation is 0.94.

Mean hardness for the section YZ is 54.1 HV5 and standard deviation is 0.75.

Measured data are included in the Appendix.

3.2. XRD results

Main goal was to find what phases can be expected in the material. Since the SEM was not available, XRD results could be good guide for the TEM observation. Comparison of the results with other papers [34], [35] shows 2 phases - α Cu and Fe_3Al κ . There is a lot of noise. Highest intensities are for the YZ section (fig. 3.2) but the peaks and noise level are similar for the other samples. Angles for the disordered martensitic β' phase was calculated from TEM results and 2θ are equal to 50.6° (corresponding to $hkl=100$) and $74.5^\circ(101)$. That is not exactly where the peaks are on the graph of fig. 3.1 (49.46° and 73.01°), but the inaccuracy in distance measurements on DP from TEM can cause difference up to 3° . On the other hand κ_1 phase was not observed on TEM so the peaks are based only on results from [34].

Angles for α were calculated $42,74^\circ(111)$, $49,76^\circ(200)$, $73,03^\circ(220)$ and $88,5^\circ(311)$.

Phase	Calculated value [°]	Measured value [°]	(<i>hkl</i>)
α	42.74	42.74	111
	49.76	49.62	200
	73.03	72.95	220
	88.5	88.43	311
β'	50.6	49.46	100
	74.05	72,95	101
κ	-	38.38	100
	-	44.09	101
	-	64.15	200
	-	72.95	420

Table 3.1.: Measured and calculated angles for different phases.

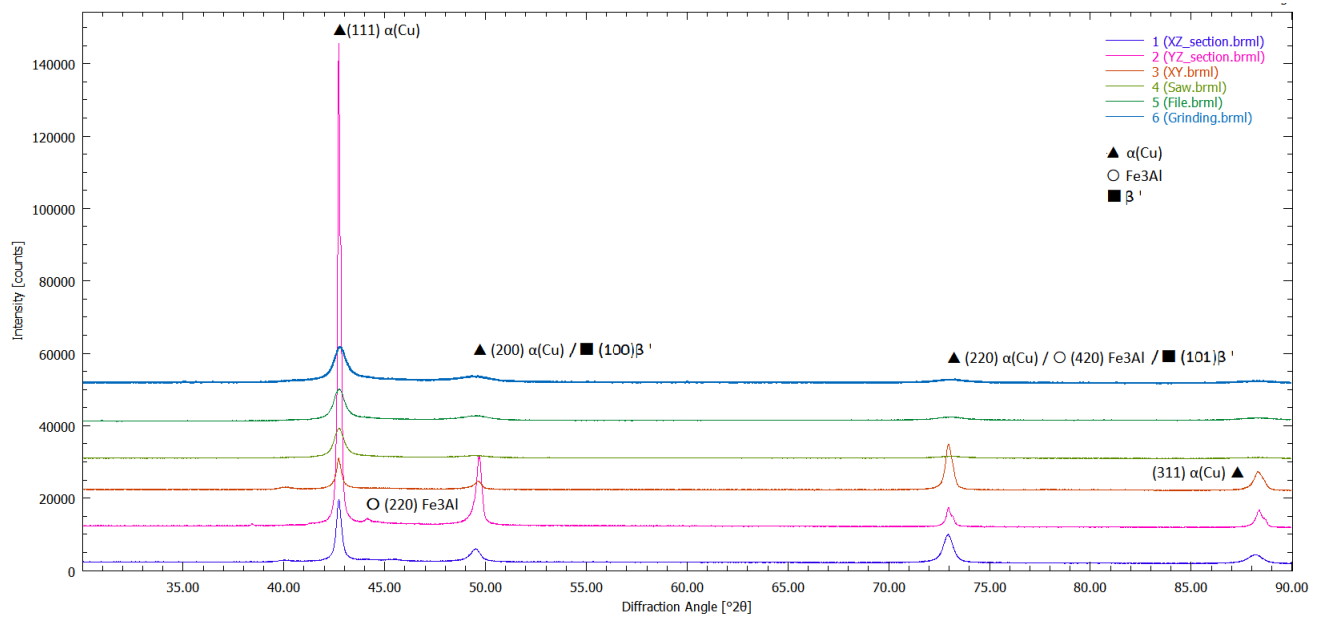


Figure 3.1.: XRD results for 3 solid samples and 3 powder samples

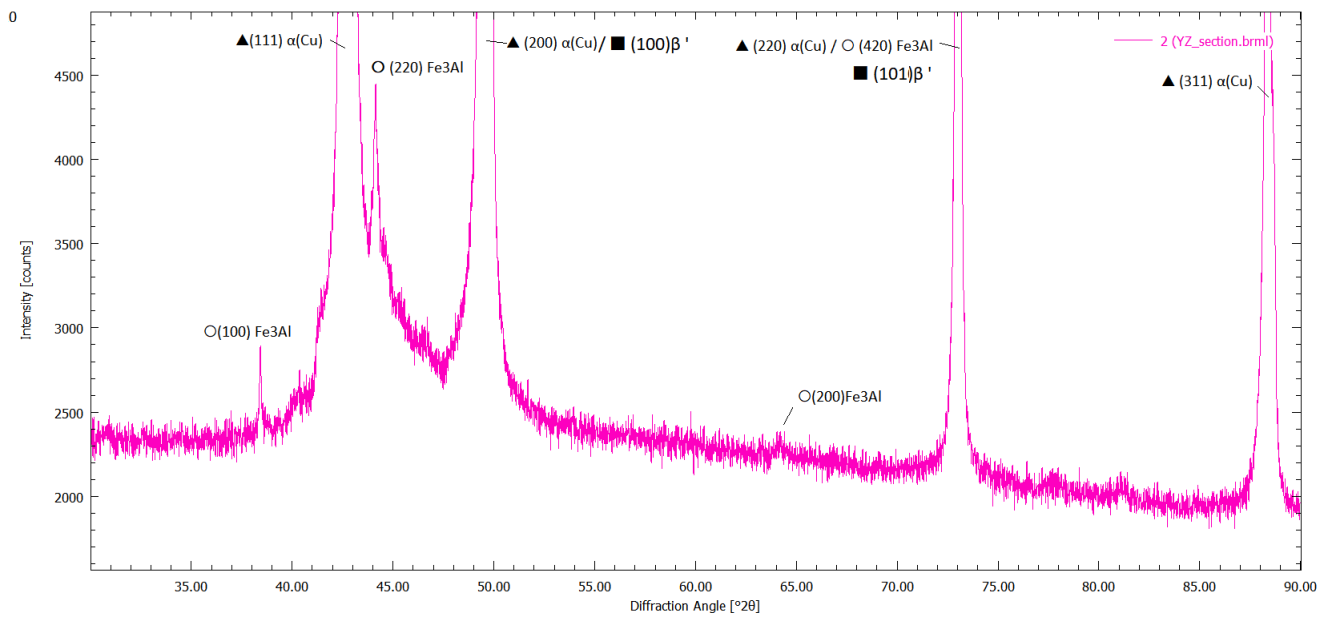


Figure 3.2.: Detail XRD results sample 2 - YZ section

3.3. Results from the light microscope

On some samples with proper finish and under certain angle, one can observe weld pools with naked eye (fig. 3.3). These weld pools are harder to find on the LM and with higher magnification it is almost impossible. At some parts of the weld pools, there are the finer grains in different orientation just next to the coarser grains with higher amount of α Cu phase. This difference could cause different deflections of the surface (see fig. 3.7). Thickness of the layer is around 0.95mm

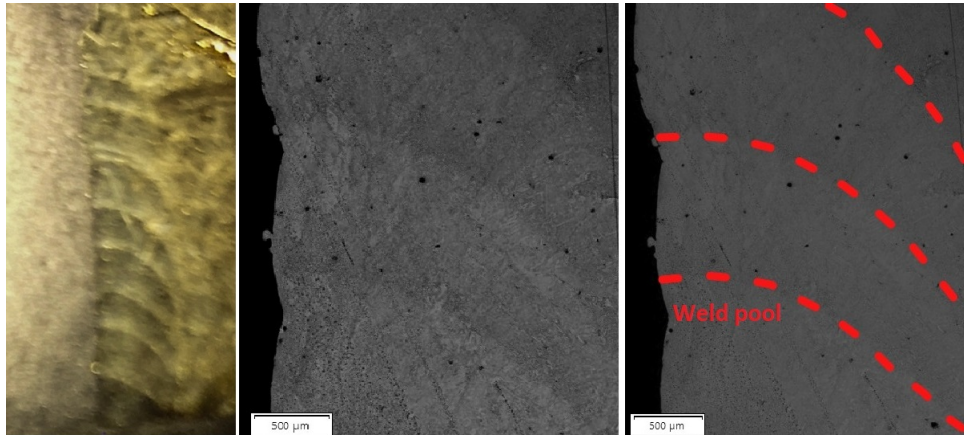


Figure 3.3.: A) Photo of the weld pools B) Weld pools on the LM C) Depicted lines of the melt pools for the picture B)

Welding defects

Multiple samples were examined and one representative is shown in fig.3.4. Area of the investigated sample was 14.2 mm^2 and around 550 pores were identified. Size of the smallest was around $2.8 \times 10^{-6} \text{ mm}^2$ and the largest was $4.2 \times 10^{-3} \text{ mm}^2$. Total area of the pores was $1.67 \times 10^{-2} \text{ mm}^2$, that is 0.16% of entire area of the investigated sample. There are no continuous networks of the pores, so the mechanical properties will not be significantly decreased.

In one case larger weld defect was uncovered (see fig. 3.5).

3.3.1. Micro-structure

Micro-structure investigation with the LM shows that grain size is changing along the surface. In fig. 3.6 typical part of the surface without any porosity is depicted. Approximately 67% of the surface shown in fig. 3.6 is α phase. Grain size of the α phase is from 0.006mm in length up to 0.07mm. In fig. 3.6 α is etched white.

Martensitic disordered β' is approximately on 32.5% of the surface and the grains are of a needle shape.

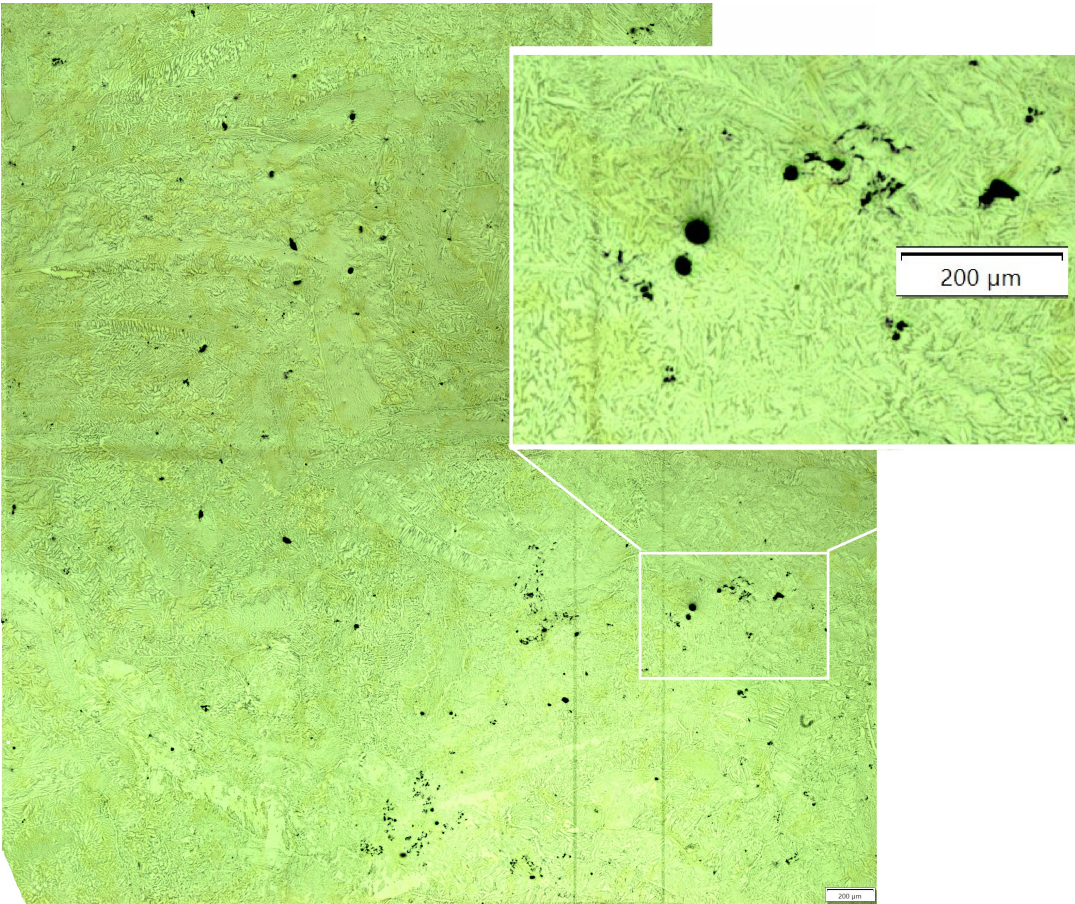


Figure 3.4.: LM picture of the surface with porosity (black particles). Circular pores possibly from shielding gas and non circular from scanning faults.



Figure 3.5.: Larger weld defect 21mm x 4mm.

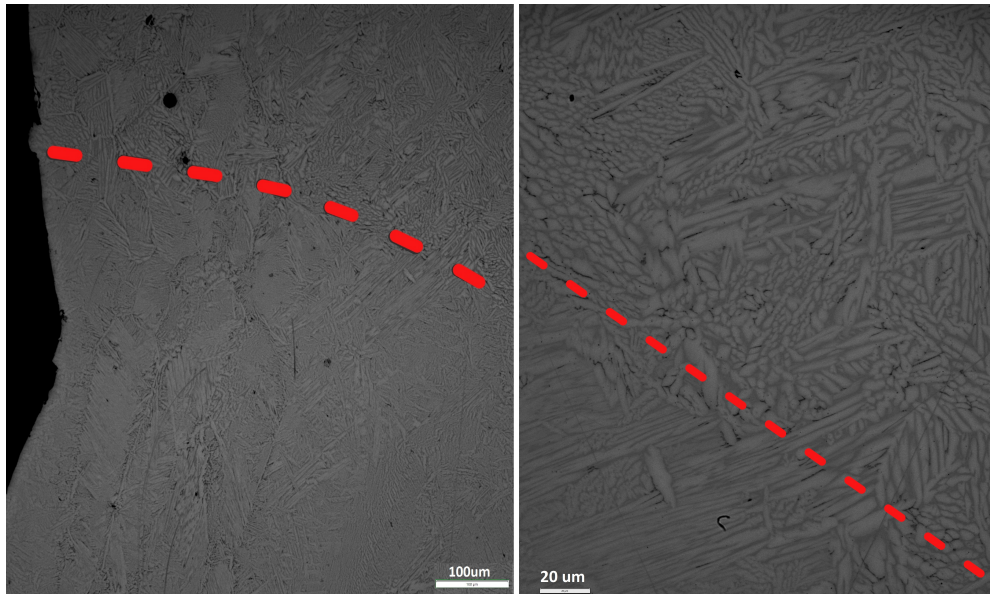


Figure 3.6.: Different magnification of weld pool boundary - different orientation and larger amount of αCu phase is probably causing visibility of the boundary.



Figure 3.7.: White parts of the picture are αCu , dark lamellar are β' and dark dots are pores or κ_1 .

3.4. SEM results

Due to the unsolved defect on UiS SEM, one sample was investigated in Oslo, but the results were not satisfactory, maybe due to bad preparation. Unfortunately, it was not possible to try one more sample. Chemical analysis confirms the chemical composition with the one supplied by NAM company.

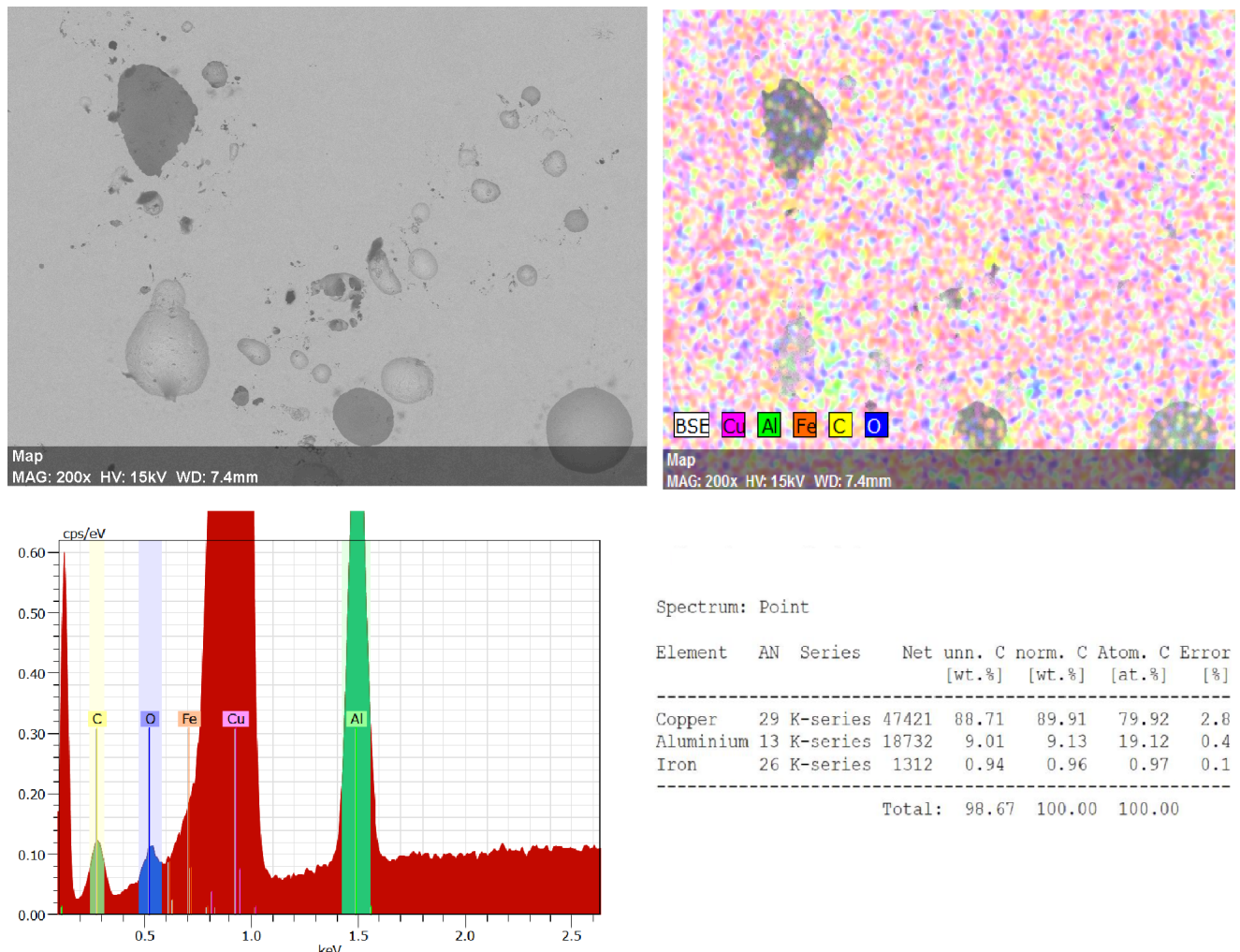


Figure 3.8.: SEM Surface picture, BSE image and chemical composition from one sample supplied by Oslo university.

3.5. TEM results

Two out of three expected phases were found. The third one, κ is not present very often and together with sample size for TEM, it is possible that we have not seen it. TEM investigation was carried out on the as-build sample, XY-section. Most of the surfaces that were investigate belongs to the Cu_3Al α phase. Dislocations and spherical precipitates were observed (see fig. 3.9). These precipitates differ according to the Al and Fe content [41] and have average diameter of 68nm, but in this work no proof of the content was obtained and this should be further investigated.

On the DP, diffusion lines are obvious that are probably caused by these precipitates and ordering phenomena. Typical surface of α phase is in the fig. 3.10 together with two diffraction patterns. Average a value calculated from multiple DP is 3.66Å.

In fig. 3.11 one can see the martensitic β' region and the DP showing the structure of the disordered martensite.

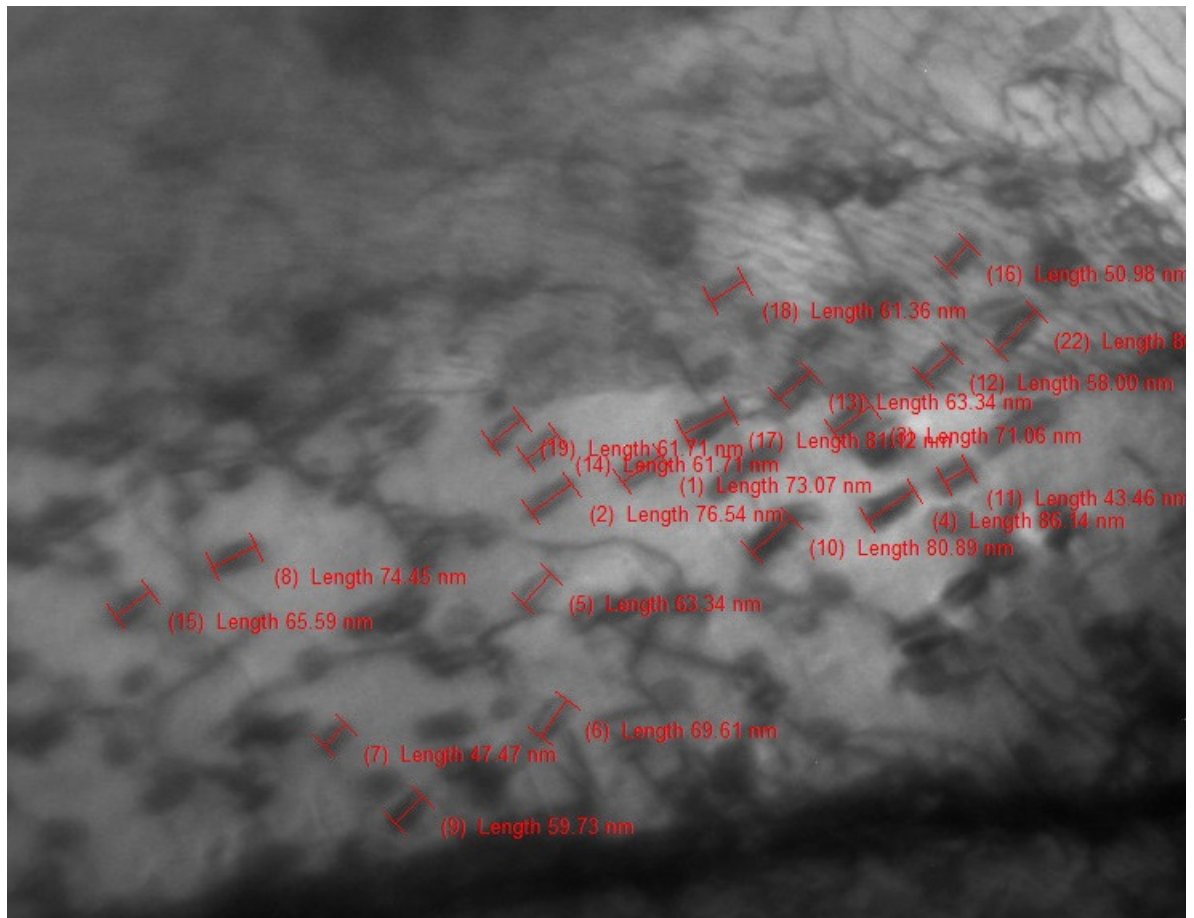


Figure 3.9.: Spherical coherent precipitates in α Cu phase

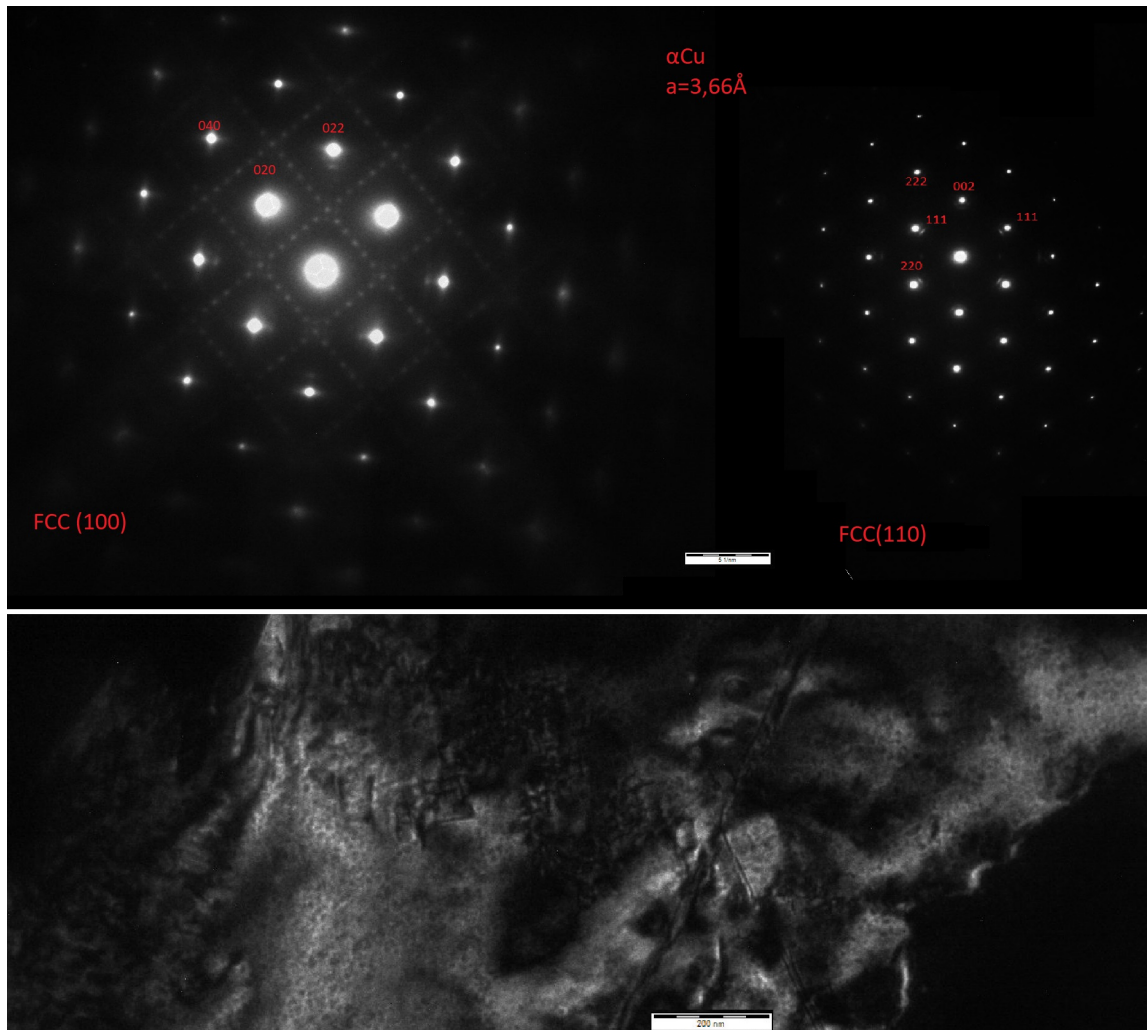


Figure 3.10.: Typical DP for the αCu phase. Right DP belongs to the surface (lower picture). In the lower picture, dislocations can be observed. Average a value calculated from multiple DP is 3.66\AA .

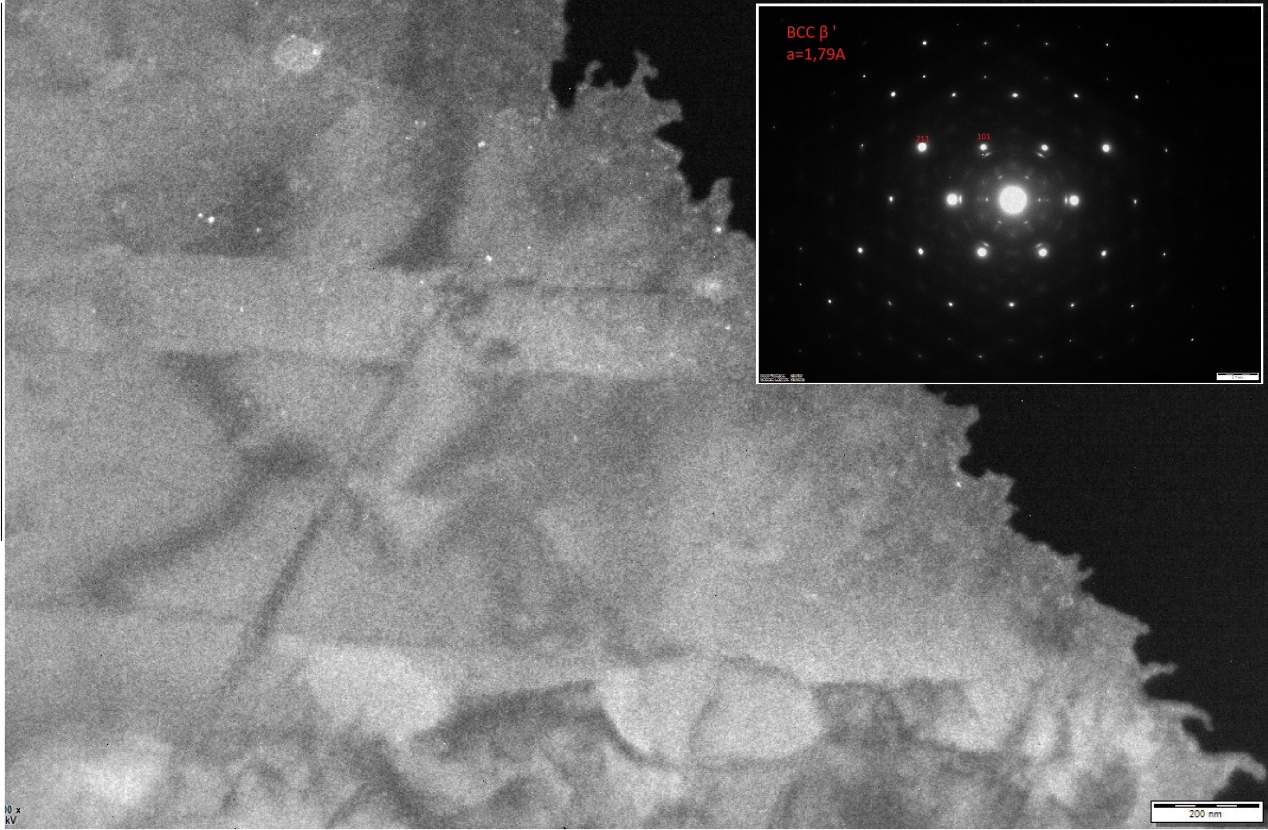


Figure 3.11.: Surface of the β phase together with diffraction pattern. Average a value was calculated as 1.79Å.

4. Conclusion

Mechanical and micro-structural properties of DED printed aluminium bronze (Al9.4Fe1Cu) were studied and compared with other present research. Material was printed in two thicknesses 0.9mm and 1.5mm and no heat treatment was applied. During the work some samples with larger pores were found, but mostly the structure was only with small amount of porosity. All the material supplied was a scrap material, the bigger cracks might be the reason, why it was not used as a final product.

Hardness of the Al-bronze was measured in all three planes. Average hardness was 52.6 HV5. Maximum hardness was in the YZ plane and the minimum hardness was in XZ plane.

Multiple samples were studied with the light microscope and the grain structure and composition was compared with the existing papers. Considering fast cooling rates during DED and chemical composition, it was concluded that three main phases should be expected. Largest portion of the surface - 67% - is the α phase. This FCC Cu phase is white etching and for slower cooling rates decompose into β . Lattice parameter was calculated to be 3.66Å, which is more than expected (3.64Å) but the calculation was made from *.jpeg files and that can bring some inaccuracy.

Second phase that is present is the β' . Al content and cooling rates strongly affect type of β phase that is created. In our study BCC disordered martensite with lattice parameter a equal to 1.79Å was found. This phase is of a needle shape and is dark etching.

From the XRD results and literature also κ phase should be present in form of Fe₃Al precipitation that are in α and β but it was not seen/confirmed on the TEM. It was maybe observed on the LM as black dots. The γ_2 was not observed.

During the TEM investigation, multiple precipitates and dislocations were observed. Dislocations were mainly in α phase and were caused by stress introduced during the cooling of the material.

4.1. Future work

It was not possible to obtain or produce material for further testing of mechanical properties, but tensile and other mechanical test for samples printed in various scanning directions would be recommended.

Micro-structural properties should be further studied using scanning microscope. That will help to investigate grater surface of the structure. Elemental chemical composition analysis using energy-dispersive X-ray spectroscopy (EDS) could bring great results. Observation using electron-backscatter-diffraction (EBSD) maps would show grain size, grain orientation and grain boundaries.

During the TEM analysis multiple precipitates in both α and β phase were observed but remain unrecognized. Information from SEM analysis might bring necessary information that would help with describing these precipitates.

References

- [1] Sarat Singamnen, Yifan LV, Andrew Hewitt, Rodger Chalk, Wayne Thomas, David Jordison. *Additive Manufacturing for the Aircraft Industry: A Review*. Journal of Aeronautics and Aerospace Engineering, In: . DOI: 10.4172/2329-6542.1000214. In: . [2019-10-20]
- [2] Samuel Clark Ligon, Robert Liska, Jurgen Stampfl, Matthias Gurr, Rolf Mulhaupt. *Polymers for 3D Printing and Customized Additive Manufacturing*. Journal of Chemical Review [2017], DOI: <https://pubs.acs.org/doi/pdf/10.1021/acs.chemrev.7b00074>
- [3] Anton Wiberg. *Towards Design Automation for Additive Manufacturing : A Multidisciplinary Optimization approach*. Linkoping University, Department of Management and Engineering, Linkoping, 2019.
- [4] Petrat, Torsten and Brunner-Schwer, C. and Graf, Benjamin and Rethmeier, Michael. *Microstructure of Inconel 718 parts with constant mass energy input manufactured with direct energy deposition*. Procedia Manufacturing [2019], . DOI: 10.1016/j.promfg.2019.08.033
- [5] *WHAT IS DIRECTED ENERGY DEPOSITION (DED)?*. TWI [2021], <https://www.twi-global.com/technical-knowledge/faqs/directed-energy-deposition>
- [6] Bin Qian, Zhijian Shen. *Laser sintering of ceramics*. Journal of Asian Ceramic Societies [2013], DOI: 10.1016/j.jascer.2013.08.004
- [7] S.M.H. Hojjatzadeh, Niranjan Parab, Wentao Yan *Pore elimination mechanisms during 3D printing of metals*. Researchgate [accessed May 2021], DOI: 10.1038/s41467-019-10973-9
- [8] Gaizka Garechana, Rosa RÃo-Belver, Inaki Bidosola, Ernesto Cilleruelo-Carrasco. *A method for the detection and characterization of technology fronts: Analysis of the dynamics of technological change in 3D printing technology*. Journal Plos One [2019], DOI: 10.1371/journal.pone.0210441
- [9] *Copper - Specifications, Properties, Classifications and Classes*. AZO materials [May 2005], <https://www.azom.com/article.aspx?ArticleID=2856>
- [10] *Copper - Specifications, Properties, Classifications and Classes*. AZO materials [June 2002], <https://www.azom.com/article.aspx?ArticleID=1446>
- [11] *Allotropy of Iron: Thermodynamics and Crystal Structures | Metallurgy*. AZO materials [accessed 5 2021], <https://www.engineeringenotes.com/metallurgy/iron/allotropy-of-iron-thermodynamics-and-crystal-structures-metallurgy/25727>
- [12] *Bronzes*. Copper Development Association [accessed 5 2021], <https://copperalliance.org.uk/about-copper/copper-alloys/bronzes/>
- [13] Ivan Richardson. *Guide to Nickel Aluminium Bronze for Engineers*. Copper Development Association [January 2016], https://www.copper.org/applications/marine/nickel_al_bronze/pub-222-nickel-al-bronze-guide-engineers.pdf

- [14] *Equilibrium Diagrams Selected copper alloy diagrams illustrating the major types of phase transformation*. Copper Development Association, CDA Publication No 94, [1992], <https://copperalliance.org.uk/uploads/2018/03/pub-94-equilibrium-diagrams-pdf.pdf>
- [15] *Types of Aluminium Bronze*. The Hendrix Group inc [accessed 5 2021], <https://hghouston.com/archive/material-property-data/copper-and-copper-alloys/aluminum-bronze/aluminium-types>
- [16] *Optickymikroskop*. 1 lekarske fakulty a Univerzity Karlovy [January 2021], https://www.wikiskripta.eu/w/Opticky_mikroskop
- [17] *NVERTED METALLURGICAL MICROSCOPE GX53*. Viontec, [accessed May 2021], <https://www.viontecmall.com/product/metallurgical-microscope-gx53/>
- [18] *The difference between SEM and TEM*. ThermoFischer [accessed 5 2021], <https://www.thermofisher.com/no/en/home/materials-science/learning-center/applications/sem-tem-difference.html>
- [19] Prof. Dr. Peter Moeck *Electron Microscopy*. Portland State University [accessed 5 2021], <http://web.pdx.edu/~pmoeck/phy381/Topic3B-SEM-Total.pdf>
- [20] Jitka Kopecka, Petra Salamunova. *Elektronova mikroskopie EM*. Laborator pripravy nano a mikromaterialu [accessed May 2021], http://fchi.vscht.cz/files/uzel/0010367/0060c_WNDwtRSE3JLAEA.pdf?redirected
- [21] *Scanning electron microscope*. Wikipedia [accessed 5 2021], https://en.wikipedia.org/wiki/Scanning_electron_microscope
- [22] *Scanning Electron Microscope (SEM)*. Bioscience Notes [June 2017], <https://www.biosciencenotes.com/scanning-electron-microscope-sem/>
- [23] Tadeas Manka. *COMPARISON OF THE IMAGING CAPABILITIES OF THE TRANSMISSION AND SCANNING ELECTRON MICROSCOPE*. BRNO UNIVERSITY OF TECHNOLOGY [May 2014], https://www.copper.org/applications/marine/nickel_al_bronze/pub-222-nickel-al-bronze-guide-engineers.pdf
- [24] Miroslav Karlik *Transmisni elektronova mikroskopie*. Katedra materialu FJFI CVUT [2005], https://nanoed.tul.cz/pluginfile.php/603/mod_resource/content/1/TEM_05_Karlik.pdf
- [25] *Transmission Electron Microscopy (TEM)*. Warwick [accessed May 2021], <https://warwick.ac.uk/fac/sci/physics/current/postgraduate/regs/mpagswarwick/ex5/techniques/structure>
- [26] *JEM-2100 Electron Microscope*. JEOL [accessed May 2021], <https://www.jeol.co.jp/en/products/detail/JEM-2100.html>
- [27] *BASICS OF X-RAY DIFFRACTION*. Thermo ARL [1999], <https://old.vscht.cz/clab/RTG/dokumenty/thermo/xrd/Introduction%20to%20powder%20diffraction.pdf>
- [28] Pavla Capkova *RTG v materialovem vyzkumu*. Universita J.E. Purkyne v Usti nad Labem [2011], http://www.kmt.tul.cz/edu/podklady_kmt_magistri/MSS/Vyukove_texty_XRD.pdf
- [29] Lokilech *RTG v materialovem vyzkumu*. Wikipedia [accessed May 2021], <https://commons.wikimedia.org/w/index.php?curid=908099>

- [30] *HV zkouska tvrdosti* . SPS zengrova [accessed May 2021], https://www.spszengrova.cz/wp-content/uploads/2020/04/KOM_3_11_SPU-mereni_tvrdosti_2.pdf
- [31] *Metco 51NS*. Oerlikon metco [accessed May 2021], <https://mymetco.oerlikon.com/en-us/product/metco51ns>
- [32] Pawee Kucita *The development of a wear resistance aluminium bronzes (Cu-Al-Fe) coating*. University of Southampton [October 2016], <https://eprints.soton.ac.uk/403720/>
- [33] J.L. Murray *The aluminium-copper system*. Int Met Rev [1985], DOI: <https://doi.org/10.1179/imtr.1985.30.1.211>
- [34] Donghong Ding, Zengxi Pan, Stephen van Duin, Huijun Li, Chen Shen. *Fabricating Superior NiAl Bronze Components through Wire Arc Additive Manufacturing*. Materials 9(8) [3 August 2016], DOI: 10.3390/ma9080652
- [35] Shuiyuan Yang, Yu Su, Cuiping Wang, Xingjun Liu. *Microstructure and properties of Cu Al Fe high temperature shape memory alloys*. Materials Science and Engineering B [2014], <https://doi.org/10.1016/j.mseb.2014.02.001>
- [36] *Directed Energy Deposition*. Procada [accessed May 2021], <https://www.procada.se/technology.html>
- [37] David Daniel McNamara. *How do eclogites deform in subduction and collision zones? An Alpine study*. Researchgate [2009], DOI: 10.13140/RG.2.2.31622.06727
- [38] *Fyzikalni zaklady vedy o materialu*. MUNI.cz [accessed June 2021], <https://www.ped.muni.cz/wphy/fyzvla/>
- [39] Adrita Dass, Atieh Moridi. *State of the Art in Directed Energy Deposition: From Additive Manufacturing to Materials Design*. Coatings [29 June 2019], <https://www.mdpi.com/2079-6412/9/7/418/pdf-vor>
- [40] Jan Ketil Solberg, Vidar Hansen, Andreas Delimitis *INTRODUCTION TO TRANSMISSION ELECTRON MICROSCOPY*. UiS Stavanger [2018]
- [41] A. Hauet, A. Bigot and D. Blavette *TEM investigation of iron segregation modes in CuAlFe dilute alloys*. Microsc. Microanal. Microstruct. 5 [1994] page 203

A. Appendix



	Inspection Certificate EN 10204 - 3.1	Oerlikon Metco Europe GmbH Spreestrasse 2 D-65451 KELSTERBACH Phone: +49 6142 6033 0 Fax: +49 6142 6033 400																																																									
Nordic Additive Manufacturing AS BG 100 Raufoss Industripark 2830 RAUFLOSS NORWEGEN	Shipping Doc/Date 800584340 / 17.12.2019	Page 1																																																									
Customer PO: Sture H Sørli PO: 200341634 Product: 1000330 METCO 51NS POWDER 5# Quantity: 45,000 LB Lot No: 490819																																																											
<table border="0" style="width: 100%; border-collapse: collapse;"> <thead> <tr> <th style="text-align: left;">Characteristic</th> <th style="text-align: left;">Inspection Method</th> <th style="text-align: left;">Value</th> <th style="text-align: left;">Unit</th> </tr> </thead> <tbody> <tr> <td colspan="4">Chemical Analysis</td> </tr> <tr> <td>Al</td> <td>ICP-OE Gen. Procedu</td> <td>9,42</td> <td>WT%</td> </tr> <tr> <td>N</td> <td>IGF</td> <td>0,005</td> <td>WT%</td> </tr> <tr> <td>Cu</td> <td>Balance</td> <td>89,38</td> <td>WT%</td> </tr> <tr> <td>Fe</td> <td>ICP-OE Gen. Procedu</td> <td>1,10</td> <td>WT%</td> </tr> <tr> <td>T.A.O.</td> <td>ICP-OE Gen. Procedu</td> <td>< 0,10</td> <td>WT%</td> </tr> <tr> <td>O</td> <td>IGF</td> <td>0,041</td> <td>WT%</td> </tr> <tr> <td colspan="4">Sieve Size</td> </tr> <tr> <td>+100 mesh (150 µm)</td> <td>ASTM B214 (SIEVE)</td> <td>0,0</td> <td>WT%</td> </tr> <tr> <td>+120 mesh (125 µm)</td> <td>ASTM B214 (SIEVE)</td> <td>4,2</td> <td>WT%</td> </tr> <tr> <td>-120 +325 mesh</td> <td>ASTM B214 (SIEVE)</td> <td>94,8</td> <td>WT%</td> </tr> <tr> <td>-100 +120 mesh</td> <td>ASTM B214 (SIEVE)</td> <td>4,2</td> <td>WT%</td> </tr> <tr> <td>-325 mesh (45 µm)</td> <td>ASTM B214 (SIEVE)</td> <td>1,0</td> <td>WT%</td> </tr> </tbody> </table>	Characteristic	Inspection Method	Value	Unit	Chemical Analysis				Al	ICP-OE Gen. Procedu	9,42	WT%	N	IGF	0,005	WT%	Cu	Balance	89,38	WT%	Fe	ICP-OE Gen. Procedu	1,10	WT%	T.A.O.	ICP-OE Gen. Procedu	< 0,10	WT%	O	IGF	0,041	WT%	Sieve Size				+100 mesh (150 µm)	ASTM B214 (SIEVE)	0,0	WT%	+120 mesh (125 µm)	ASTM B214 (SIEVE)	4,2	WT%	-120 +325 mesh	ASTM B214 (SIEVE)	94,8	WT%	-100 +120 mesh	ASTM B214 (SIEVE)	4,2	WT%	-325 mesh (45 µm)	ASTM B214 (SIEVE)	1,0	WT%	Approved Specifications: B50TF161-S8 Cl. A Supplier Code 59090 MSRR9507/24 Issue 2 DMR 33-046 Indice A		
Characteristic	Inspection Method	Value	Unit																																																								
Chemical Analysis																																																											
Al	ICP-OE Gen. Procedu	9,42	WT%																																																								
N	IGF	0,005	WT%																																																								
Cu	Balance	89,38	WT%																																																								
Fe	ICP-OE Gen. Procedu	1,10	WT%																																																								
T.A.O.	ICP-OE Gen. Procedu	< 0,10	WT%																																																								
O	IGF	0,041	WT%																																																								
Sieve Size																																																											
+100 mesh (150 µm)	ASTM B214 (SIEVE)	0,0	WT%																																																								
+120 mesh (125 µm)	ASTM B214 (SIEVE)	4,2	WT%																																																								
-120 +325 mesh	ASTM B214 (SIEVE)	94,8	WT%																																																								
-100 +120 mesh	ASTM B214 (SIEVE)	4,2	WT%																																																								
-325 mesh (45 µm)	ASTM B214 (SIEVE)	1,0	WT%																																																								
<p>Material was tested and released by Oerlikon Metco (US) Inc., Troy, MI unless otherwise stated.</p> <p>Trace element analysis and any required metallurgical analysis is performed by a qualified Nadcap approved laboratory. Any element reported as less than 50 ppm is considered as a trace element except for Carbon, Sulfur, Oxygen, Nitrogen and Hydroger Details available upon request.</p>																																																											
<small>It is hereby certified that the material described above has been inspected, and conforms to all applicable requirements of the contract order and specifications referenced on this certificate. This certificate shall not be reproduced except in full without the written approval of Oerlikon Metco. The recording of false, fictitious, or fraudulent statement or entries on this certificate may be punished as felony under the federal law. This material is being supplied in accordance with the Quality System at Oerlikon Metco Europe GmbH which is an ISO 9001:2008 Certified Vendor. This material is supplied according to the quality requirements of the customers purchase orders. This inspection certificate meets the requirements of EN10204:2005 3.1 (Inspection Certificate), 2.2 (Test Report) or 2.1 (Certificate of Compliance with the Order).</small>																																																											
By  <small>Quality Assurance representative on behalf of</small> Joern Lindner																																																											

Figure A.1.: Certificate of the powder used for the production of the tested samples.

1	51,52	Mean	51,676	
2	50,54	STD	0,838002917	
3	50,7			
4	51,75			
5	51,98			
6	52,2			
7	52,49			
8	52,46			
9	50,47			
10	52,65	XZ section		
1	54,61	Mean	52,261	
2	52,39	STD	0,942555038	
3	52,39			
4	51,54			
5	51,16			
6	51,5			
7	52,2			
8	52,41			
9	51,98			
10	52,43	XY section		
1	55	Mean	54,062	
2	53,9	STD	0,743726353	
3	54,45			
4	52,69			
5	53,41			
6	54,55			
7	54,08			
8	53,85			
9	53,58	YZ section		
10	55,11			

Figure A.2.: Results of the Vickers hardness test - load 5kg for 10s.